Naval Research Reviews

Office of Naval Research
Two / 1992
Vol XLIV

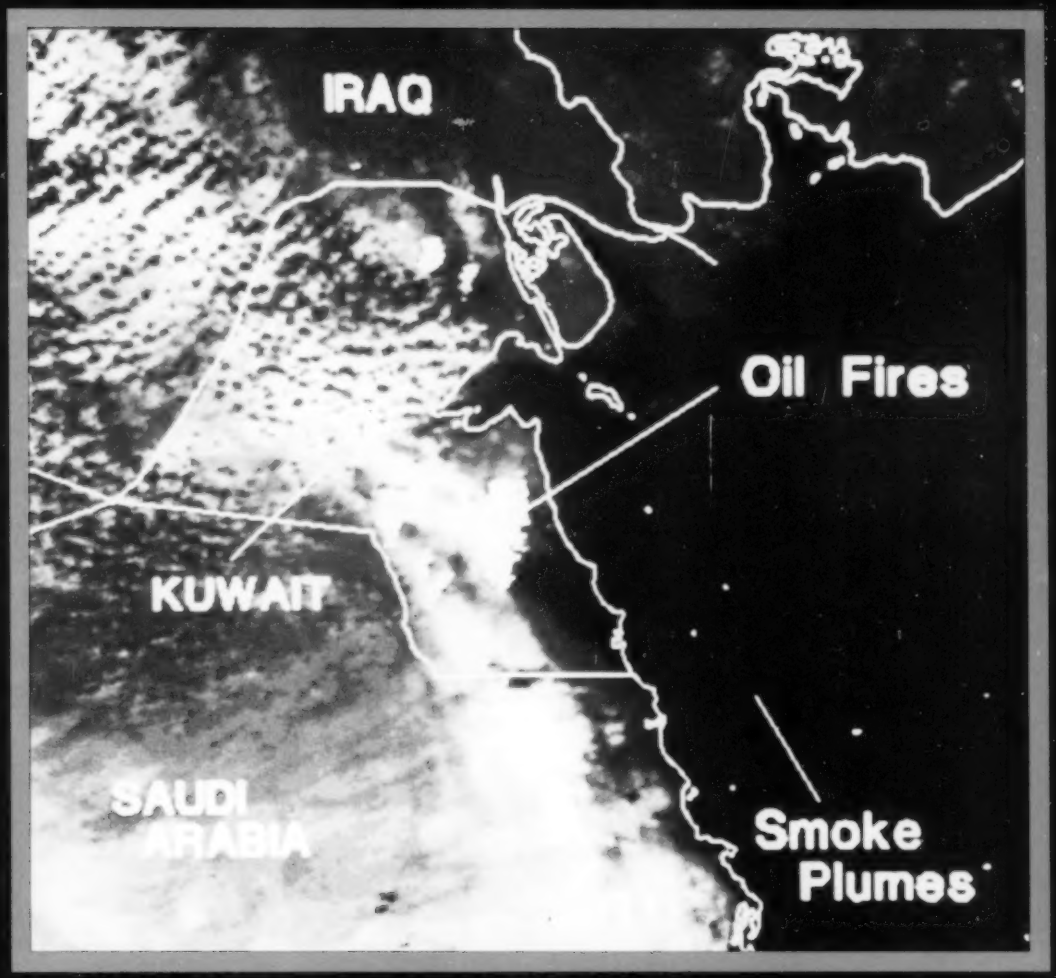

A Robot Ancestor

"Shakey," a mobile robot with TV "eyes", tactile sensors, an optical range finder and an elementary navigation system, connected to a large computer, performed autonomously back in 1969. The Stanford Research Institute created Shakey with Office of Naval Research funding. Later, the Advanced Research Projects Agency (ARPA) and the National Aeronautics and Space Administration (NASA) joined the program. The field of robotics or artificial intelligence has the goal of endowing machines with those characteristics that are called "intelligence" when exhibited by people. Some day robots may substitute for man in exploring the deep oceans and in performing tasks in hostile or hazardous environments. Shakey could plan and execute simple tasks such as finding objects and manipulating them in the laboratory while avoiding obstacles. The robot performed "smart" activities involving perception, planning, model-building, and problem solving.

In 1949, when ONR created a Computer Branch in the Mathematical Sciences Division, it was the first government agency to dedicate a group of scientists to support computer and information research. Many of the early concepts which ONR pioneered have become standard techniques or important areas of research such as: time sharing, artificial intelligence, systolic computing, neural networks, machine learning, and connectionist computing.

Today the overall objective of the ONR program in robotics is to advance the scientific basis for understanding intelligent, sensor-based mechanical systems. Robotic achievements span the disciplines of computer science, mathematics, mechanics, materials, electronics, and psychology. From the perspective of computer science, however, dramatic progress in robotic capabilities is expected to come about only to the extent that research in robotics is closely linked to research in artificial intelligence. Both robotics and artificial intelligence share a common set of basic research issues: knowledge acquisition, knowledge representation, and automated reasoning. Robots then combine these capabilities with advances in locomotion and actuation to yield robust, intelligent behavior.

Naval Research Reviews

Office of Naval Research
Two / 1992
Vol XLIV

Articles

2
The Underwater Sounds of Precipitation
Lawrence A. Crum, Ronald A. Roy, Andrea Prosperetti

13
Laser Cooling Atoms To Ultra-Low Temperatures In A Magnetic Field
Harold Metcalf, Peter Reynolds

22
Multispectral Image Enhancement Reveals Kuwaiti Oil Plumes
Thomas F. Lee, James Clark Maureen Thompson

27
Thermoacoustic Refrigeration for Space Applications
Steven L. Garrett, Jay A. Adeff Thomas J. Hofler

Departments

21
Profiles in Science

36
Research Notes

CHIEF OF NAVAL RESEARCH
RADM William C. Miller, USN

DIRECTOR
Dr. Fred Saalfeld

CHIEF WRITER/EDITOR
William J. Lescure

SCIENTIFIC EDITORS
Dr. Robert J. Nowak
Dr. J. Dale Bultman

MANAGING EDITOR
Norma Gerbozy

ART DIRECTION
Typography and Design
Desktop Printer, Arnold, MD

About the Cover

A satellite image from the NOAA-11 orbiting satellite shows the Kuwaiti oil fires on 2 March 1991. The white spots over Kuwait indicate the burning oil fields, and the black plume represents smoke which is moving downwind. (See article starting on page 22.)

Naval Research Reviews publishes articles about research conducted by the laboratories and contractors of the Office of Naval Research and describes important naval experimental activities. Manuscripts submitted for publication, correspondence concerning prospective articles, and changes of address, should be directed to Code OPARI, Office of Naval Research, Arlington, VA 22217-5000. Requests for subscriptions should be directed to the Superintendent of Documents, U.S. Government Printing Office, Washington, DC 20403. *Naval Research Reviews* is published from appropriated funds by authority of the Office of Naval Research in accordance with Navy Publications and Printing Regulations. NAVSO P-35.

The Underwater Sounds of Precipitation

Lawrence A. Crum and Ronald A. Roy, National Center for Physical Acoustics, University of Mississippi
Andrea Prosperetti, Department of Mechanical Engineering, Johns Hopkins University

Abstract

The Office of Naval Research has supported a research program at our respective institutions for the past few years in the general area of bubble-related ambient noise in the ocean. In the course of our study of this topic, we came to discover some interesting things about the underwater sounds produced by the impact of rain, hail and snow on the surface of the sea. This paper describes the physical processes that produce these acoustic emissions and shows that a major portion of precipitation noise is caused by the injection of gas bubbles into the liquid by the impact of rain drops, hail stones and snow flakes.

Introduction

The distinctive sound of a raindrop striking a puddle of water is familiar to us all. It is one of those unique sounds in nature that is immediately recognizable. The sound of a pebble tossed into a quiet pond has a similar uniqueness and, to most of us, even evokes a sense of tranquillity. The soft, acoustic environment of falling snow is the very essence of stillness. We have examined these forms of precipitation and have found that the noise produced when they impact a water surface has at its origin an oscillating gas bubble. The study of the underwater sounds produced by precipitation is part of our general study of bubble-related ambient noise in the ocean, which has been supported by the Ocean Acoustics Program of the Ocean Sciences Directorate, Office of Naval Research.

Historical Background

Precipitation plays an important role in the climate of a particular region and, more generally, in our total global environment. Its occurrence has relevance to latent heat release, upward mass flux, and the spatial organization of convection. Thus, knowledge of the rate of rainfall and its geographical distribution is of major interest.

Due to rain's spatial and temporal discontinuity, accurate measurements are difficult even over land because rain gauges at discrete sampling sites can give misleading values. Radar can provide a more complete coverage, but its general use is restricted to the developed countries. Rainfall measurements over the ocean where – according to estimates[1] – 80% of the earth's precipitation occurs, are yet more difficult to obtain. Typically, the few weather stations located on the ocean are on islands, a circumstance that leads to an inadequate sampling of the global distribution. Shipboard measurements suffer problems such as contamination by sea spray, platform instabilities, and spatially-biased sampling.

Satellite-based, remote sensing of the earth's environment probably provides the highest promise for adequate global rainfall monitoring. Yet, such measurements are time-consuming, costly, and suffer the important limitation of "ground-truth," i.e., adequate land- or sea-based calibration.

It is against this background that Walter Munk's idea of using the underwater noise produced by rain to monitor rainfall rates remotely over the ocean can be appreciated. His suggestion was taken up by Nystuen, Scrimger, and others[2-4] in the early eighties with very unexpected and intriguing results.

In the open literature the first brief mention of the underwater noise of rain occurs in the famous 1948 paper by Knudsen *et al.*[5]. The first study of the spectrum of rain noise was reported by Heindsman *et al.* in 1955 up to a frequency of 10 kHz[6]. This study was later duplicated and the results confirmed by Bom[7]. In the frequency range investigated it was found that the spectrum of rain was approximately flat and its level increased with rainfall rate. In the early eighties, Lemon *et al.*[8] tried to infer rainfall rates from measured underwater sound but, although they were able to identify correctly the intervals of their acoustic records corresponding to rainfall, their attempt was quantitatively inconclusive.

Our attention was drawn to this problem – and, more generally, to the study of precipitation noise-in the course of a search for bubble-related sources of underwater sound that we undertook in the mid-eighties. While it had been appreciated before that bubbles could contribute to underwater noise (see, *e.g.*,[9]), the suggestion that they may be responsible for most of the wind-dependent oceanic ambient noise is recent[10,11] and has not been exhaustively explored yet. In the context of rain, the possible role of bubbles was pointed out by Franz in 1959[12] who however-erroneously, as we shall see – discounted it.

If an isolated bubble of radius R is produced in the ocean, it will oscillate at its natural frequency f which can be estimated from a formula obtained by Minnaert in 1933 in the course of a study of the babbling sounds of brooks and streams[13]:

$$f = \frac{1}{2\pi R}\sqrt{\frac{3\gamma P_0}{\rho}} \qquad (1)$$

Here P_0 is the ambient pressure, ρ the liquid density, and γ (equal to 7/5 for air) is the ratio of specific heats of the gas. A useful mnemonic approximation to (1) for P_0 = 1 bar is fR ~3 kHz x mm. Very short-lived large bubbles (radius of the order of a few cm) may perhaps be produced under heavy sea conditions by the impact of splashes on the water surface, but certainly are far less common than smaller bubbles in the range from millimeters to tens of microns which are produced in great abundance by breaking waves. Below this size range, bubbles are not readily generated – it would require too much energy concentrated in too small a scale. In normal conditions one expects therefore the acoustic emissions of individual bubbles to lie in the range between 1 and 100 kHz. Lower frequencies are possible through the collective oscillations of bubble clusters, or clouds, as shown in Refs.[14-15] but we need not concern ourselves with these cooperative effects here.

Rain Noise

There is a variety of mechanisms that can lead to the production of individual, isolated gas bubbles in the ocean. One of the more intriguing ways is through the impact of a water drop, produced by ocean spray or falling precipitation. Franz[12] discovered in 1959 that occasionally when a water drop strikes the water, the air-filled cavity produced by the impact entrains a gas bubble, which produces a relatively large sound. He discounted this bubble as an important noise source, however, because entrainment was observed to occur only rarely in his studies of rainfall noise. More recently, however, some measurements have been made that led a group of us to reexamine this phenomenon.

Figure 1.

Underwater noise spectra of rain (a-c), hail and snow for wind speeds greater than 1.5 m/s. The spectrum level is expressed in dB relative to 1μPa²/Hz. Rain rates: a, 1.1 mm/hr; b, 0.29 mm/hr; c, 0.13 mm/hr. Wind speeds: a, 2.7 m/s; b, 2.7 m/s; c, 2.23 m/s. [Taken from Scrimger[3].]

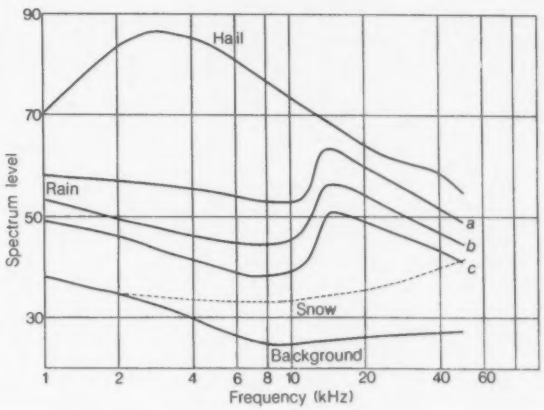

In 1985, Scrimger published a pioneering study of the underwater noise produced by precipitation[3]. By installing a hydrophone near the bottom of a lake in British Columbia, he obtained measurements of the underwater acoustic spectrum of rain, hail and snow, more by chance than by design. These measurements, reproduced in Figure 1, provided the motivation for our attempts to determine the physical sources for these spectra.

One can observe from these data that all forms of precipitation produce underwater sounds significantly above the background level. Furthermore, each form also has a distinct signature and maximum in its frequency response. (Because of limitations in the bandwidth of the hydrophone used, the snow measurements do not show a relative maximum, but since the level can not keep increasing indefinitely with frequency, these data indicate that it must exist.)

As shown in Figure 1 and in an additional series of measurements made by Nystuen[2] and by Scrimger *et al.*[4] a distinct peak occurs in the rain noise spectrum. This peak has a very rapid rise, (60 dB/octave), and a distinctive fall-off with

frequency above the peak (9 dB/octave). Such unique behavior suggests an underlying, well-defined, physical mechanism.

This unique sound spectrum enticed us to look at the noise produced by an individual drop impact in hopes that we would be able to discern aspects of its behavior that would lead to a more general explanation of the phenomenon[16-19]. Shown in Figure 2 is a pressure-time trace of the sound produced by an individual drop impacting a plane water surface obtained by Pumphrey *et al.*[18]

This trace was obtained by displaying the output of a broadband hydrophone on a storage oscilloscope. Note that there are two sounds produced. The first, small bump on the trace is that due to the direct impact of the drop with the water surface; the second, a much more intense sound, delayed in time by about 24 ms, is a damped sinusoid indicative of the ringing of a harmonic oscillator. If one examines the sinusoid in more detail, it is found to have a frequency of about 10 kHz and the damping characteristic of an oscillating gas bubble of approximately 300 microns in radius. This bubble is barely visible to the naked eye but it is the source of the overwhelming majority of the noise.

Figure 2.

Oscilloscope traces of the sounds produced by a water drop of 3.0 mm diameter impacting at a velocity of 2.0 m/s on a plane surface in a water tank. The upper trace shows the whole process, with the initial impact occurring at a time of about 8 ms and the bubble sound at 32 ms. The lower trace is an expansion along the time axis of a part of the upper one and shows the bubble sound in greater detail. [Taken from Pumphrey et al.[18].]

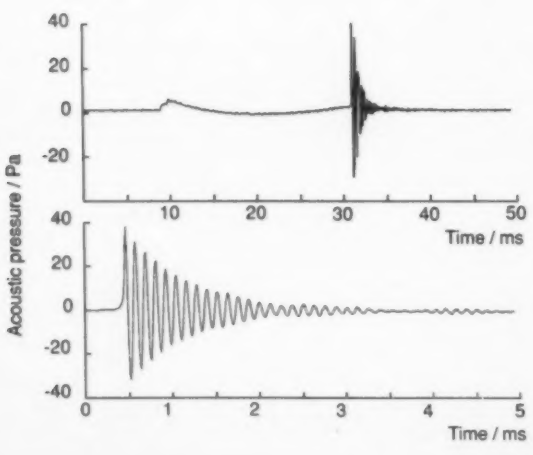

Figure 3.

Selected frames from a high-speed movie film, showing regular entrainment of bubbles. The original film was made at a speed of 2000 frames per second. The water drop (seen in Figure 3a) had a diameter of about 3 mm and an impact velocity of 2 m/s. The line down the right hand side of the film is an oscilloscope trace showing the acoustic pressure amplitude; in Figures 3h and 3i it was too faint to reproduce well and was touched up by hand. The damped sine wave in Figures 3h and 3i has a frequency of about 9 kHz. Times after impact for each frame are as follows: (a) -3 ms, (b) 0 ms, (c) 2 ms, (d) 6.5 ms, (e) 14.5 ms, (f) 20 ms, (g) 20.5 ms, (h) 21 ms, (i) 21 ms, (j) 35.5 ms. [Taken from Prosperetti et al.[17].]

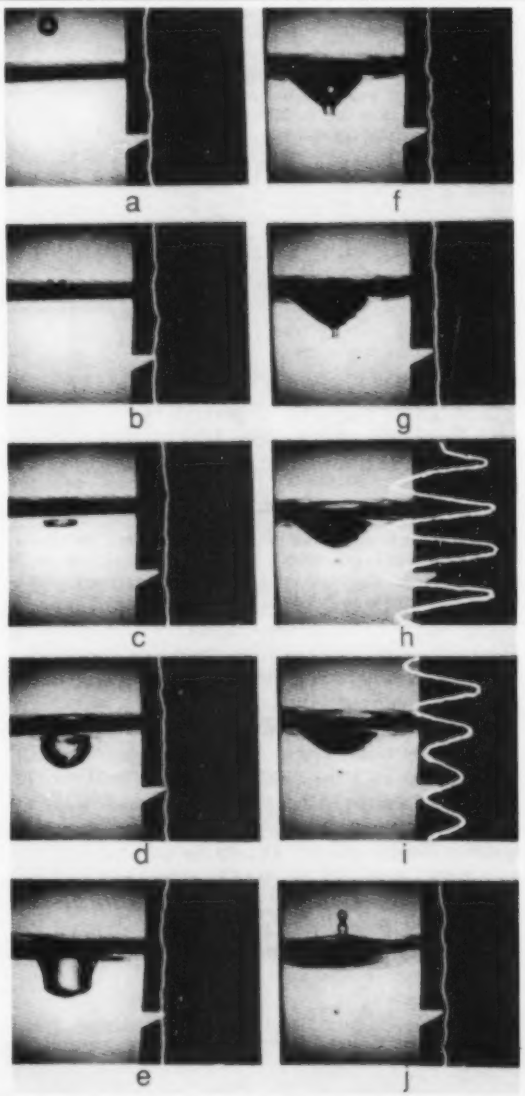

Because it had been previously reported that the 15 kHz peak (actually the peak frequency reported by different investigators varies somewhat between 14 - 16 kHz) was due to the water-hammertype pressure generated by the drop impact itself[2] and, because we kept observing that the entrained bubble noise was so much stronger, we made an effort to study the impact and entrainment process in more detail. Shown in Figure 3 are high-speed photographs of the dynamics of a drop impacting on a liquid surface, accompanied on the film by the pressure-time history of the sounds produced by the impact. It is seen quite clearly from the film sequence that almost all the sound is produced, in this particular case, by the entrained gas bubble.

Although the noise spectrum of rainfall is composed of individual drop impacts, the drops are also of many different sizes. We next tried to make measurements of the noise spectra of many different drop sizes by generating artificial rainfall. There are many devices that have been developed to simulate rainfall but we found that, by using a spray from a hose, we could obtain drop-size distributions roughly characteristic of natural rainfall. Furthermore, by directing this spray from a height in order that we would obtain terminal velocity for the drops, we could reproduce the naturally occurring rainfall acoustic spectrum.

Shown in Figure 4 are the results of examining this artificial rainfall in a laboratory tank ($1m^3$) as displayed in both the time and frequency domain. The upper trace shows that the time history is replete with damped sinusoids with decay constants appropriate to gas bubbles; the bottom trace shows that an average power spectrum of 200 such traces gives the typical natural rainfall spectrum. Note that this graph is taken directly from the oscilloscope, which can plot only a linear spectrum, while the spectrum shown in Figure 1 is shown on a log scale. If these data are converted to such a scale, the spectra are surprisingly similar. These experiments pointed

Figure 4.

A sound-pressure trace produced by a spray of water falling onto a large tank of water (above) and an average power spectrum of 200 such traces (below). Here the reference level is arbitrary. In comparing this artificial rainfall spectrum with the natural one in Figure 1, note that the frequency scale in this figure is linear. [Taken from Pumphrey et al.[18].]

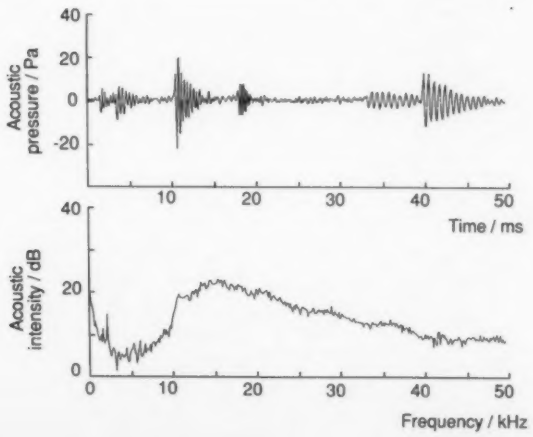

Figure 5.

(a) Conditions necessary for bubble entrainment. Regular entrainment occurs in the shaded region in the center of the figure, irregular entrainment occurs (very approximately) in the striped region at the top of the graph. Most of the data points used to draw the boundary of this region are off the edge of the graph. The line at the left is the terminal velocity curve for raindrops, and the two vertical lines are at the drop diameters at which the terminal velocity curve passes through the regular entrainment region, i.e., 0.8 and 1.1 mm. (b) Drop-size distributions for three different rain showers. This shows that a large proportion of the drops in a typical rain shower are in the size range for which the terminal velocity curve intersects the shaded region, i.e., between the two vertical lines. Hence, many raindrops fulfill the conditions for regular entrainment. The units on the ordinate are: number of drops in a 0.1 mm size range striking an area of 50 cm^2 in a time of 90 s. [Taken from Pumphrey et al.[18] and Scrimger et al.[4].]

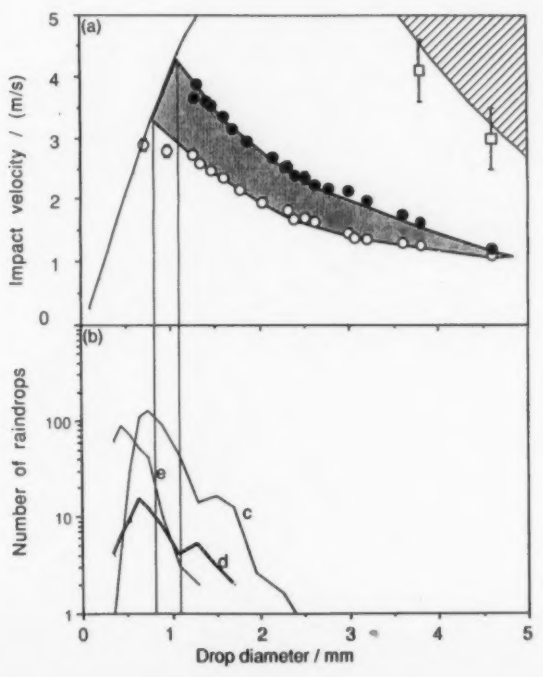

Figure 6.

Computer simulation of regular entrainment. The surface shown represents the water surface after drop impact. The drop size and velocity input data correspond to the conditions observed in Figure 3. The first set of numbers above each figure refer to the time after impact in milliseconds. Compare these times with those in Figure 3. [Taken from Oguz and Prosperetti[21].]

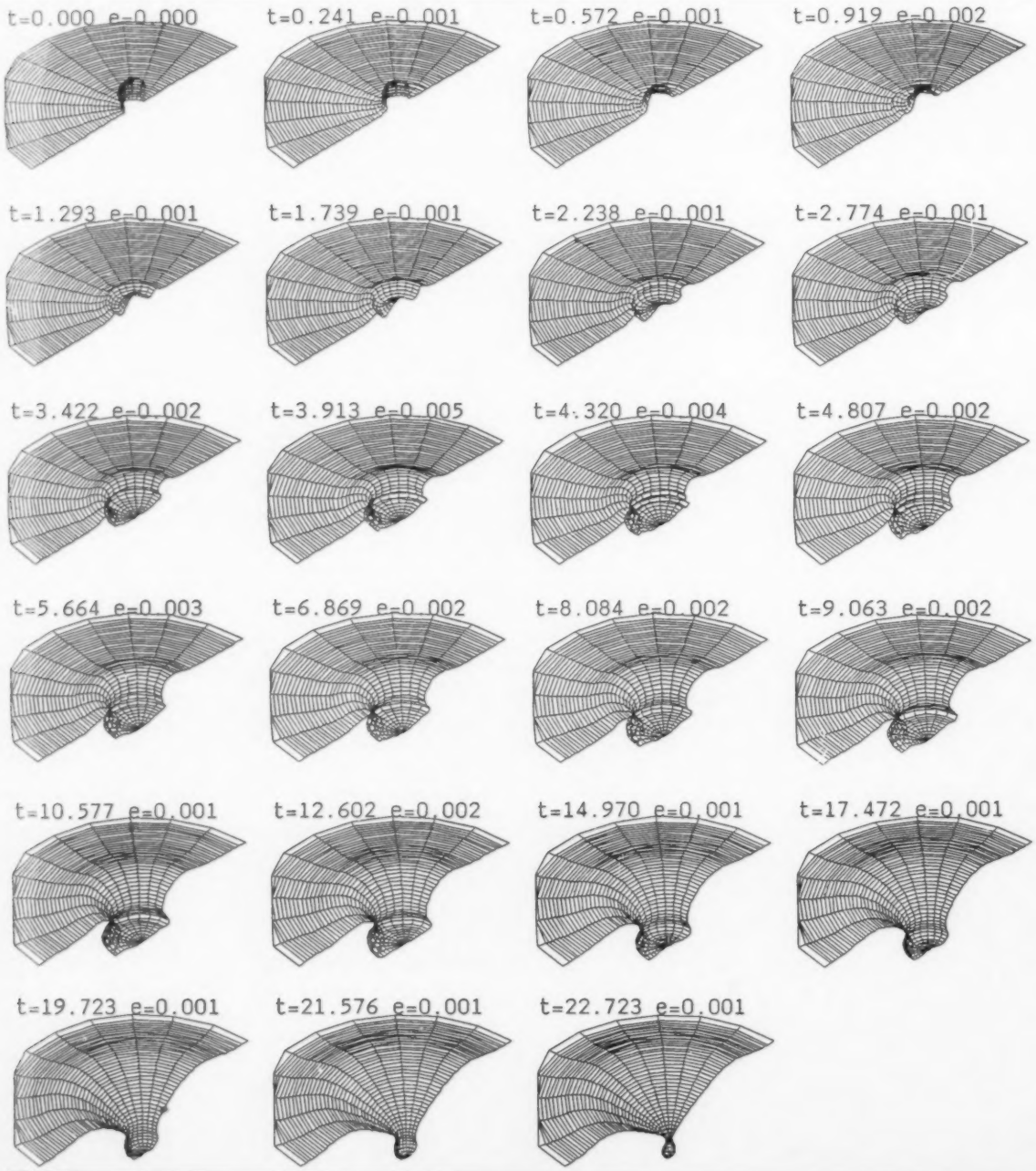

Figure 7.

Selected frames from a high-speed movie showing a drop of 3.8 mm diameter impacting at 1.5 m/s. With clean water these parameters lead to regular entrainment, as in Figure 3, but in this case a surfactant has been added to the water. The surfactant prevents a bubble from being entrained, and consequently little sound is produced. The original movie was taken at a speed of 1000 frames per second. Times after impact for each frame are as follows: (a) -9 ms, (b) -1 ms, (c 1 ms, (d) 5 ms, (e) 8 ms, (f) 13 ms, (g) 20 ms, (h) 27 ms, (i) 57 ms. [Taken from Prosperetti et al.[17].]

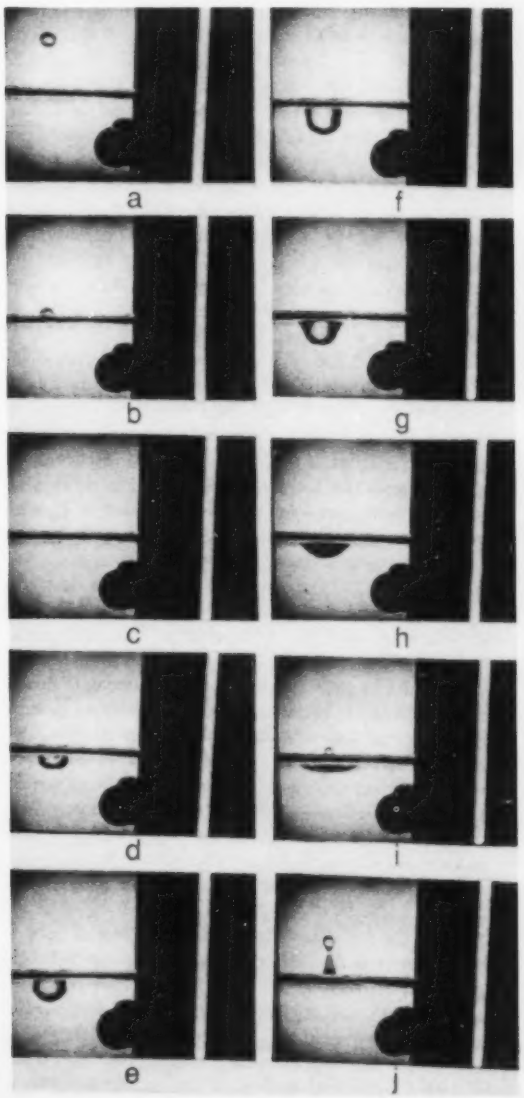

toward bubble entrainment (and subsequent bubble oscillation) as the dominant contributor to the 15 kHz peak.

In contrast to these arguments, Franz[12] and others[2] had maintained that because an impact sound is produced for each raindrop, and because bubbles are only occasionally entrained, the rainfall spectrum, including the 15 kHz peak, must be primarily due to drop impacts, with minor contributions from bubbles.

We thus sought to determine the proportion of raindrops that gave rise to bubble entrainment. Shown in Figure 5 is a result obtained by Pumphrey *et al.*[18] that is particularly revealing.

In this figure, we have examined the parameter space in which an impacting raindrop produces a bubble (i) always, (ii) never, and (iii) sometimes. The parameters of interest are the impact velocity and the drop diameter. The important, and revealing, portion of this figure is the shaded area bounded by the two curves and intersecting the terminal velocity line, shown in the upper left portion of the figure. Within the shaded region, an impacting drop produces a bubble every time (provided the impact is normal to the water surface). Pumphrey called this region "regular entrainment." The intersection of the regular entrainment region and the terminal velocity curve indicates which raindrops produce bubbles. This range of drop sizes is quite limited, from approximately 0.8 to 1.1 mm, and any acoustical study of underwater rain noise is therefore actually sensitive only to the drops in this range. Since this range is so small, one may expect a certain "universality" of rain noise, with different rain events giving rise to different noise levels, but all with the same spectral shape. Plotted on the same Figure 5 is also data from Scrimger *et al.*[4] which shows measurements of typical distributions of raindrop sizes. These data indicate that drops of the sizes required for bubble entrainment do occur in relatively large number.

The region of parameter space where regular entrainment occurs is well defined and places severe restrictions upon the hydrodynamics of the drop impact/bubble entrainment process[19-22]. A bubble is always produced within the region while it is never produced even slightly outside its upper or lower boundaries. A different type of fluid mechanics occurs in the irregular entrainment region in the upper right-hand corner. We have investigated the fluid dynamics of bubble entrainment by drop impact[21, 22] and can reproduce many of the features of the experimental curves from a direct numerical solution of the Euler equations. Figure 6 shows a sample calculation of the entrainment of a gas bubble upon the impact of a liquid drop on a plane surface. It is quite remarkable that using the basic equations of fluid mechanics, a theoretical underwater rainfall sound spectrum can be generated[22]. We call to the attention of the interested reader some analytical work on this problem by Longuet-Higgins[20].

Because surface tension forces have an influence on the shape of the crater produced by the drop on the liquid surface, which in turn gives rise to bubble entrainment, it is interesting to see the effect of the addition of a surfactant to the liquid.

Shown in Figure 7 is a sequence of photos taken from a high-speed movie of a drop impact under the same conditions as in Figure 3; however, in this case, a surface-active film was added to the host fluid. It is seen that in this case, contrary to the clean surface of the earlier figure, a bubble is not entrained.

This result led us to consider how the actual rainfall spectrum might change should a surface-active agent be present on the water surface. We received an answer to this question when our colleague Leif Bjørnø, at the Technical University of Denmark, measured the spectrum of a natural rainfall in a tank before and after adding a surfactant. Figure 8 indicates that the 15 kHz peak was completely "silenced" by the surface-active agent.

The fact that reduced surface tension changes the bubble entrainment (and thus the noise generation) process in a fundamental way can be nicely demonstrated in a bathtub. When filling the tub, observe the sound produced by the running water as air is entrained. Then, add a small amount of bath oil or other detergent. A distinct, audible change will occur.

Our studies have demonstrated rather conclusively that the 15 kHz peak in the rainfall spectrum is due to gas bubble entrainment for which the fluid mechanics define the shape of the peak. It has been suggested[2] that the unique underwater noise spectrum of rainfall could lead to its use as a remote monitor of such precipitation in areas of the ocean not covered by weather stations. Although data by Scrimger *et al.*[4] indicate an excellent correlation between rainfall rates and the amplitude of the 15 kHz peak at low wind speeds, its amplitude and shape are also very dependent upon local conditions such as wind speed, the presence and height of waves on the surface, the angle of impact of the raindrops and, most importantly, the number of drops in the critical size bandwidth that leads to regular entrainment. Although the source of the acoustic spectrum for regions outside the 15 kHz peak are still not clearly understood,[2, 23-27] these regions may provide a more reliable frequency band for the remote monitoring of rainfall. Recent results by Nystuen and Ostwald[27] are quite promising.

There are many evolutionary developments that occur in nature in which animals adapt to a specific acoustic environment.[28, 29] As a bit of an aside, but of considerable interest to us, is the notion that there may be some aquatic species, dependent upon the occurrence of rainfall, that have evolved specific adaptations that would sense the presence of this unique acoustic spectrum. Because the peak has a sharp low-pass cut-off and is relatively high in frequency, it might not be too difficult to identify anatomical adaptions that would be specific to it.

Figure 8.

Acoustic power spectra of real rain falling into clean water (closed circles) and water with detergent added (open circles). Here, the dB reference is arbitrary. [Taken from Pumphrey et al.[18].]

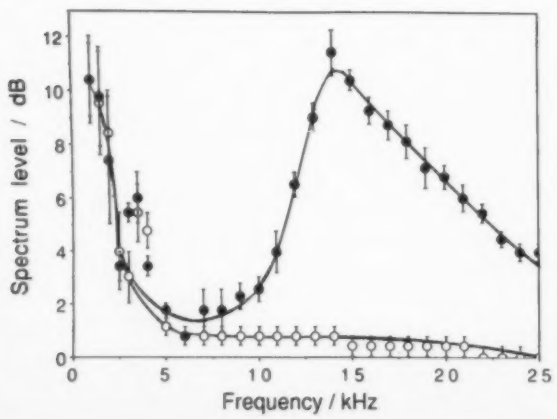

Figure 9.

Pressure history and power spectrum for artificial hailfall. The top trace shows a pressure-time recording of the impact of a polypropylene sphere of 6.0 mm diameter, dropped from a height of 2.0 m, onto a plane water surface. The damped sinusoid is indicative of the sound radiated by a gas bubble of approximately 3 mm in diameter. Not shown on this trace is the pressure spike due to the direct impact itself, which occurs several milliseconds earlier in time and with an amplitude approximately 10% of the maximum shown here. The middle trace shows the power spectrum of the top trace, and the bottom trace shows the average power spectrum of 20 such traces; ordinate scales are in arbitrary units. The arrow indicates a frequency of 2 kHz (the abcissa is frequency with a scale of 2 kHz per division) for the approximate peak in the power spectrum. Compare this laboratory spectrum of artificial hail with that for natural hail shown in Figure 1.

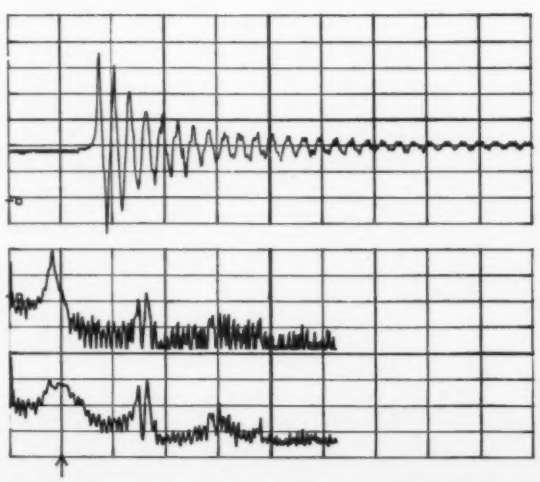

Hail Noise

Scrimger's original study indicated that a unique underwater acoustic spectrum also was generated by the impact of hailstones. Our studies of rain noise led us to believe that the impact of a hailstone would not be unlike that of a raindrop and that gas bubbles associated with the cavity opened in the water would more likely be the source of the noise than the impact itself.

Figure 10.

Frames from high speed movie of artificial hailstone impact process. The framing rate was 1000 f/s; the frames are sequential but not necessarily successive. The insert in the lower right shows the acoustic pressure measured by a hydrophone in the water beneath the impact and displayed on an oscilloscope screen. The impacting object is shown slightly above the water surface in (A) and this process is thus followed in time. Note that very little sound is associated with the impact, or with wake generation; rather, acoustic emissions occur simultaneously with the closure of the air cavity behind the sphere, and continue as this cavity oscillates. [Courtesy of Michael Nicholas.]

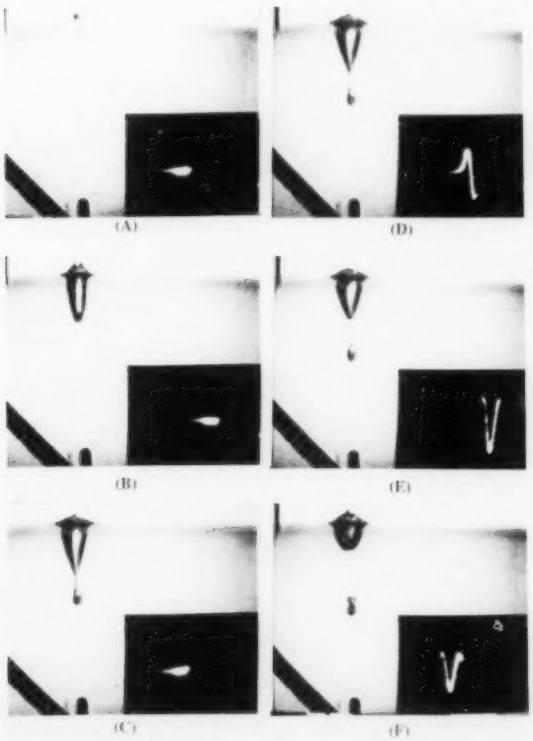

Our attempts at making artificial hailstones – due to the rarity of their natural presence in Mississippi – were reasonably successful. However, we soon found that the sound of an artificial hailstone could be easily duplicated by a polypropylene sphere, with the latter being reusable and permitting more systematic studies.[30]

Shown at the top of Figure 9 is a pressure-time trace of the impact of an artificial hailstone on a plane water surface as measured by a hydrophone and displayed on an oscilloscope. Note that this trace is very similar in appearance to that shown in Figure 2 for an impacting water droplet, indicating that a gas bubble has been produced that radiates energy in the course of damped oscillations. Also shown in this figure is the average power spectrum for a number of these impacts, showing a relatively broad peak at about 2 kHz. Note that this peak is consistent with that obtained by Scrimger *et al.*[4] for natural hail.

Following the success in our rainfall studies, we have also filmed the impact of our artificial hailstones with a water surface while monitoring the acoustic pressure generated during this process. As expected, the impact of the stone itself produces little sound; it is the breakup of the cavity into gas bubbles that gives rise to acoustic emissions as demonstrated in Figure 9. These cinephotographic results are shown in Figure 10 and illustrate quite graphically the importance of gas bubble production in the noise generation process.

As always in such studies, nature continues to provide lovely subtleties. For example, if the sphere is wetted, the dynamics of the contact line as it enters the water is very different than if the surface is dry. Figure 11 shows that for the same size sphere, dropped from the same height, into the same tank of water, a dry sphere produces a significant acoustic emission while a wet one produces little measurable sound. We learned, after performing these measurements, that Worthington[31] observed as early as 1908 that the sound produced by impacting solid objects depended on the surface characteristics, including wetness and dryness.

Snow Noise

We were intrigued by Scrimger *et al.*'s report that snowfall gave rise to underwater acoustic emissions. We have demonstrated to our satisfaction that gas bubbles are involved in the impact of rain and hail; could they also be associated with snow?

As things go in science, it was a chance occurrence that led us to an answer. One evening in late December, after preparing for some measurements of rainfall on the roof of our laboratory, it began to snow. With a hydrophone in a garbage pail on the roof of a laboratory in the dim light of an evening snowfall in Mississippi – how rare an occurrence – we saw snowflakes gently settle onto the water surface, and saw on the oscilloscope damped sinusoid traces, characteristic only of gas bubbles. Shown in Figure 12 is a typical example. Rather

remarkably, this acoustic emission shows an initial growth, and then a subsequent decay. With hundreds of traces obtained during three different snowfalls, this same general shape is reproduced each time.[32]

We have analyzed the decay constant of these traces, and have determined that, within experimental error, they match that associated with gas bubble oscillations.[32] Why the growth, before the decay? Consider the following hypothesis: When the snowflake strikes the water, it has very little vertical momentum. The surface tension forces that give rise to capillarity immediately engulf the snowflake encapsulating air (or trapped air is released from within the ice crystals). Since the gas bubble is now contained in a small water protrusion above the water surface, it radiates inefficiently, but as the surface tension forces pull it below the surface, its subsequent cycles can radiate at a higher amplitude, thus giving the characteristic shape of the acoustic emission.

Because the bandwidth of our hydrophone extended to approximately 125 kHz, in contrast to that of only 50 kHz for Scrimger, Figure 13 shows that our spectrum extends out to over 100 kHz, and probably to the cut-off frequency of our own hydrophone. We plan to repeat these measurements with a higher-bandwidth hydrophone.

We noted earlier that many of us have experienced the stillness of a snow storm. Yet, were we to live underwater and be able to discern frequencies in the tens of kilohertz (as can many marine mammals), then a snow storm would not be quiet at all, but rather a shrill background of high frequency noise. At least in this realm, it's better to be human.

Figure 11.

Oscilloscope traces of the sounds produced by an impacting artificial hailstone as measured by an immersed hydrophone. The top trace shows the characteristic signal associated with bubble entrainment and subsequent oscillation; for this case the sphere's surface was dry upon impact. The bottom trace shows that under identical conditions, a sphere whose surface is wet does not produce a measurable acoustic emission.

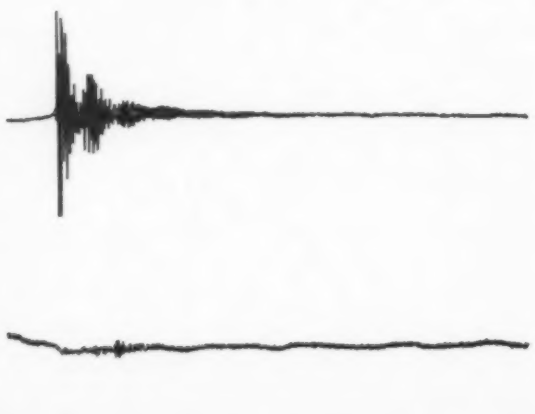

Summary

The investigation of the source mechanisms for ambient noise in the ocean has led us to an examination of the underwater noise produced by precipitation. These studies have led to the conclusion that the ubiquitous gas bubble provides the source for the acoustic emissions of rain, hail, and snow, and that under certain conditions the monitoring of this underwater noise might be used to learn more about important environmental conditions otherwise inaccessible. Finally, this work also illustrates how ONR-sponsored work often progresses from a directed study of a specific issue to the unanticipated discovery of important aspects of our natural environment. While such discoveries may initially have only scientific interest, they may also subsequently play a role in the solution of major problems.

Figure 12.

Oscilloscope traces of the sounds produced by an "impacting" snowflake onto a water surface as measured by an immersed hydrophone. These particular waveforms, with an initial positive phase, with a growth stage, and with a subsequent decay are characteristic of snowfall. Note the reproducibility of the two traces (the top trace shows a double-event). For these cases, the frequencies were on the order of 100 kHz which is associated with a gas bubble of approximately 30 microns in radius. The peak amplitude of the trace as measured with a calibrated hydrophone located a few centimeters from the impact was on the order of 2-3 Pa.

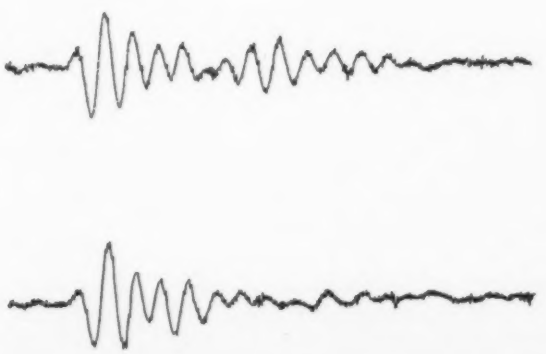

Acknowledgement

We wish to gratefully acknowledge the financial support of the Office of Naval Research, Ocean Sciences Directorate, the helpful suggestions of Dr. Marshall Orr, Program Manager, Ocean Acoustics, the contributions of Dr. Hugh Pumphrey, who was responsible for acquiring most of the rain data, of Dr. Michael Nicholas for the hail data, and of Dr. Hasan Oguz who made decisive contributions to the numerical simulations of rain drop impact.

Biographies

Lawrence A. Crum attended the US Naval Academy and Ohio University where he received his Ph.D. in 1967. He has held positions at the US Naval Academy, Harvard University and the University of Mississippi where he is currently F.A.P. Barnard Distinguished Professor of Physics. Professor Crum was Visiting Professor of Physics at University College Cardiff, Wales in 1977-78 and was on a Fulbright Fellowship at Guy's Hospital Medical School in London in 1985-86. He is a Fellow of the Acoustical Society of America and of the American Institute of Ultrasound in Medicine. Currently he is Interim Director of the National Center for Physical Acoustics at the University.

Andrea Prosperetti graduated in Physics from the University of Milano and obtained a Ph.D. in Engineering Science at the California Institute of Technology in 1974. After 1975 he was Assistant and then Associate Professor of Physics and Fluid Mechanics at the University of Milano and the Politecnico of Milano, and Professor of Mechanics at the University of Cagliari. Since 1985 he is Professor of Mechanical Engineering at the Johns Hopkins University where he has also chaired the Department. Professor Prosperetti spent the Fall 1991 semester as Mitsubishi Visiting Professor at the University of Tokyo. He is a Fellow of the Acoustical Society of America.

Ronald A. Roy received his BS degree from the University of Maine, his MS from the University of Mississippi and his Ph.D. from Yale University in 1987 where he was an ONR Graduate Fellow. He was formerly Director of Research and Development at Apfel Enterprises in New Haven, CT, before accepting his present position at the University of Mississippi where he is Research Assistant Professor of Mechanical Engineering and Research Scientist at the National Center for Physical Acoustics.

Figure 13.

Average power spectrum for the "impact" of snowflakes onto a plane water surface in a large tank. The ordinate is in db with an arbitrary reference; the abcissa is frequency with each division corresponding to 50 kHz. The cutoff frequency for the hydrophone was about 125 kHz; thus, the high frequency fall-off of the spectrum is probably due to limitations in the hydrophone response.

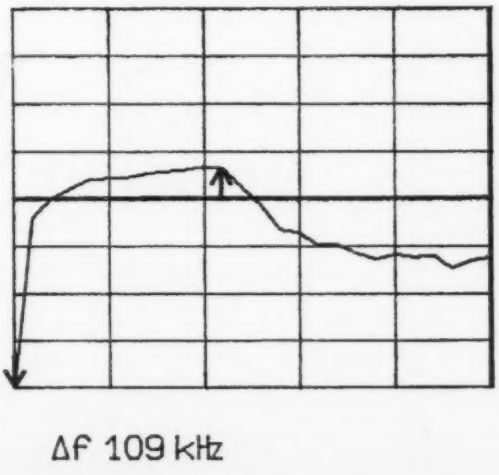

References

1. S. Q. Kidder and T. K. Vonder Haar, "Seasonal oceanic precipitation frequencies from Nimbus 5 microwave data," J. Geophys. Res. **82**, 2083 (1977).
2. J. A. Nystuen, "Rainfall measurements using underwater ambient noise," J. Acoust. Soc. Am. **79**, 972-982 (1986).
3. J. A. Scrimger, "Underwater noise caused by precipitation," Nature **318**, 647-649 (1985).
4. J. A. Scrimger, D. J. Evans, G. A. McBean, D. M. Farmer and B. R. Kerman, "Underwater noise due to rain, hail and snow," J. Acoust. Soc. Am. **81**, 79-86 (1987).
5. V. O. Knudsen, R. S. Alford and J. W. Ensling, "Underwater ambient noise," J. Marine Res. **1**, 410-429 (1948).
6. T. E. Heindsman, R. H. Smith, and A. D. Arneson, "Effect of rain upon underwater noise levels", J. Acoust. Soc. Am. **27**, 378 (1955).
7. N. Bom, "Effect of rain on underwater noise level," J. Acoust. Soc. Am. **45**, 150 (1968).
8. D. D. Lemon, D. M. Farmer, and D. R. Watts, "Acoustic measurements of wind speed and precipitation over a continental shelf," J. Geophys. Res.**89**, 3462 (1984).
9. G. M. Wenz, "Acoustic ambient noise in the ocean: Spectra and sources," J. Acoust. Soc. Am. **34**, 1936-1956 (1962).
10. A. Prosperetti, "Bubble-related ambient noise in the ocean," J. Acoust. Soc. Am. **84**, 1042-1054 (1988).

11. W. M. Carey and D. Browning, "Low frequency ocean ambient noise: Measurements and theory," in Natural Mechanisms of Surface Generated Noise in the Ocean, ed. by B. R. Kerman, C. Kluwer, Dordrecht, Netherlands , pp. 361-376. (1988)

12. G. J. Franz, "Splashes as sources of sound in liquids," J. Acoust. Soc. Am. **31**, 1080-1096 (1959).

13. M. Minnaert, "On musical air bubbles and the sound of running water," Phil. Mag. **16**, 235-248 (1933).

14. S. W. Yoon, L. A. Crum, A. Prosperetti and N. Q. Lu, "Collective oscillations of a bubble cloud," J. Acoust. Soc. Am. **89**, 700 (1991).

15. A. Kolaini, R. A. Roy and L. A. Crum, "Acoustic emissions from a bubble plume," J. Acoust. Soc. Am. **89**, 2452 (1991).

16. H. C. Pumphrey and L. A. Crum, "Acoustic emissions associated with drop impacts," in Sea Surface Sound, ed. by B.R. Kerman (Kluwer, Norwell, MA), pp. 463-483 (1988).

17. A. Prosperetti, L. A. Crum and H. C. Pumphrey, "The underwater noise of rain," J. Geophys. Res. **94**, 3255-3259 (1989).

18. H. C. Pumphrey, L. A. Crum and L. Bjørnø, "Underwater sounds produced by individual drop impacts and rainfall," J. Acoust. Soc. Am. **85**, 1518-1526 (1989).

19. H. C. Pumphrey and P. A. Elmore, "The entrainment of bubbles by drop impacts," J. Fluid Mech. **220**, 539-567 (1990).

20. M. S. Longuet-Higgins, "An analytic model of sound production by raindrops," J. Fluid Mech. **214**, 395-410 (1990).

21. H. N. Oguz and A. Prosperetti, "Bubble entrainment by the impact of drops on liquid surfaces," J. Fluid Mech. **219**, 143-179 (1990).

22. H. N. Oguz and A. Prosperetti, "The underwater noise of rain," J. Fluid Mech. **228**, 417 (1991).

23. H. C. Pumphrey and L. A. Crum, "Free oscillations of near-surface bubbles as a source of the underwater noise of rain," J. Acoust. Soc. Am. **87**, 142-148 (1990).

24. F. Laville, G. D. Abbott and M. J. Miller, "Underwater sound generation by rainfall," J. Acoust. Soc. Am. **89**, 715-721 (1991).

25. J. A. Nystuen and D. M. Farmer, "The influence of wind on the underwater sound generated by light rain," J. Acoust. Soc. Am. **82**, 270-274 (1987).

26. H. Medwin, J. A. Nystuen, P. W Jacobus, D. E. Snyder and L. H. Ostwald, Jr., "The anatomy of underwater rain noise", J. Acoust. Soc. Am. (in press).

27. J. A. Nystuen and L. H. Ostwald, Jr., "An inversion technique to measure rain using underwater sound", J. Acoust. Soc. Am. (in press).

28. T. G. Forrest, "Acoustic communication and baffling behavior of crickets," Florida Entomologist **65**, 33-44 (1982).

29. T. G. Forrest and D. M. Green, "Sexual selection and female choice in mole crickets (Scapteriscus: Gryllotalpidae): modelling the effects of intensity and mole spacing," Bioacoustics (in press).

30. M. Nicholas, R. A. Roy and L. A. Crum, "The underwater sound produced by the impact of solid objects," J. Acoust. Soc. Am. **89**, 2013 (1991).

31. A. M. Worthington, A Study of Splashes, Longmans, Green and Co., London, 1908.

32. L. A. Crum, R. A. Roy and A. Prosperetti, "The underwater noise of falling snow", J. Acoust. Soc. Am. (in press).

Laser Cooling Atoms To Ultra-Low Temperatures In A Magnetic Field

Harold Metcalf, State University of New York, Stony Brook
Peter Reynolds, Office of Naval Research

Introduction

The motion of atoms and molecules that results from their thermal energy has had a profound influence on a wide variety of laboratory measurements. The average kinetic energy of this motion is directly proportional to absolute temperature and thus can never be eliminated except at the unattainable temperature of absolute zero. Atomic velocities associated with this motion are typically 500 m/s at ordinary temperature. This high speed of free atoms, together with the variation of the speeds of different atoms from the same sample, has produced the ultimate limitation on a variety of high precision laboratory measurements.

This thermal motion of atoms currently imposes two distinct limits to ultrahigh resolution spectroscopy and atomic clocks. One of these arises from the broadening of the spectral line caused by the small interaction time between the measuring equipment and rapidly moving atoms. At 500 m/s, there are only a few milliseconds to interact with a free atom in an apparatus of reasonable size (i.e., a few meters). The other limit arises from a frequency shift caused by the relativistic time differences between reference frames in relative motion (sometimes called the second order Doppler effect; the first order Doppler effect is the familiar classical frequency shift between moving objects). If we knew the velocity of the atoms with respect to the measuring apparatus, this effect could be calculated and accommodated. But the atoms have a velocity *distribution*, characterized by the temperature of their source. Although this too can be calculated, the details of the distribution at the low velocity end depend very sensitively on the details of the source, and sometimes cannot be adequately known. A sample consisting of slowly moving or monovelocity atoms could provide a substantial improvement in spectroscopic resolution.

Such cold atoms have other uses as well. For example, there is currently much forefront atomic physics research carried out in electromagnetic traps where a variety of properties of the atoms as well as key questions in quantum mechanics and field theory may be addressed. Because these traps are so shallow for neutral atoms, atoms must be cooled considerably in order to be captured. Yet another application for a collection of slowly moving and/or monovelocity atoms would be as an ideal beam or target for a variety of low energy and/or high energy-resolution scattering experiments, chemical reaction studies, or surface studies. There are many other applications that require monoenergetic atomic beams, including sensitive beam deflection experiments for the study of quantum statistics in optical absorption and emission.

Laser Cooling and Optical Molasses

The use of electromagnetic forces to influence the motion of neutral atoms has been a subject of interest for some years. It is widely known that there is a force associated with electromagnetic radiation, colloquially known as light pressure. Because the interaction of light with matter is quantum mechanical, there is a resonance phenomenon when the light frequency is at or near the resonance frequencies of atomic transitions. The origin of this force derives from the momentum associated with light when it is scattered by atoms. In addition to energy $E = \hbar\omega$, a quantum of light carries momentum $E/c = \hbar k$ and angular momentum $\hbar$. Here ω is the angular frequency of the light, the wave vector $\mathbf{k}$ along the direction of propagation has magnitude $|k| = 2\pi/\lambda$ where λ is the optical wavelength, and the speed of light c is related to ω and k by $c = \omega/k$. When an atom absorbs light, it stores the energy by going into an excited state, it stores the angular momentum in the form of internal motion of its electrons, and it absorbs the linear momentum by recoiling from the light source with a velocity $\hbar k/m$. It is this velocity change of the atom that is of special interest here. Although $\hbar k/m$ is only a few cm/sec for typical atomic resonance frequencies in the visible region, and this is very small compared with thermal velocities, repeated scattering can be used to produce a large total velocity change. Proper control of this change can create a *velocity dependent* radiative force that can be used both to decelerate and to cool a sample of free atoms. Uniformly slowing the atoms in a beam alone would not cool it, as the variations in the velocity, i.e. $\langle v^2 \rangle - \langle v \rangle^2$, would remain unchanged.

The first laser cooling experiments used a single beam of light travelling opposite to a beam of atoms. By tuning the light below resonance, each atom has its velocity reduced by an amount that depends on its Doppler shift.[1,2] Another way to use the Doppler effect to make the radiation pressure force depend on the atomic velocity uses a pair of counterpropagating light beams to exploit the difference of radiation pressures from the two beams as seen by the moving atoms.[3,4] Again, the laser light is tuned below the moving atoms' resonant frequency. In the atom's rest frame, the laser beam travelling *opposite* to the atom's velocity is Doppler shifted closer to its resonance frequency. As a result this latter beam is preferentially scattered. Thus the radiation pressure, or scattering force, opposes atomic motion in *either* direction. This experimental arrangement is readily generalized to three dimensions. Then no matter which way an atom tries to move it feels a "viscous" drag force. This damps atomic velocities toward zero. It is thus clear why this experimental arrangement is called "optical molasses".

This damping is most effective when the Doppler shift $\mathbf{k} \cdot \mathbf{v}$ is less than the natural width γ of the atomic transition,

Figure 1.

Velocity dependence of optical damping forces for one-dimensional optical molasses. The two dotted traces show the force from each beam (with opposite Doppler shifts), and the solid curve is their sum. The straight line shows how this force mimics a pure damping force over a restricted velocity range.

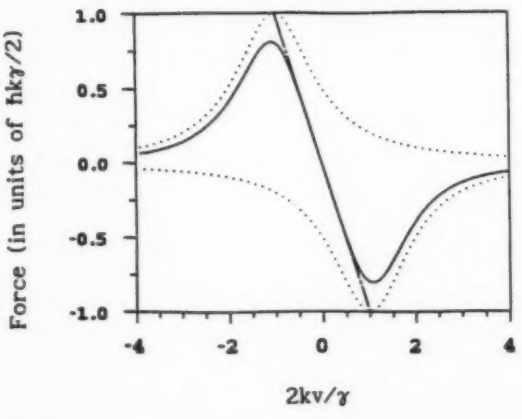

namely when $v_z \leq \gamma/k$ in the two-beam case described above, where v_z is the component of velocity along the laser beams. The velocity dependence of this force is plotted in Figure 1. In addition to the damping, there is also heating produced because the absorbed light is spontaneously re-emitted, giving the atoms a random momentum kick. The balance between the damping and the heating that arises from the directional randomness of the spontaneous emission yields a steady-state kinetic energy and temperature. Calculation of this lowest attainable temperature[5] using a model "two level atom" gives the so-called Doppler cooling limit $T_D = \hbar\gamma/2k_B$. This turns out to be approximately 140 μK for Rb ($\gamma = 1/\tau = 2\pi \times 6$ MHz for Rb).

When a group working at NIST first measured the temperatures of laser-cooled atoms in 1988, they were quite surprised to find it well *below* this Doppler limit.[6] Workers in other laboratories quickly confirmed this astounding result.[7-9] The experimental discovery of temperatures below T_D led to new theoretical models of optical molasses[10,11] that depended upon the multiple sublevel structure of real atoms. The new cooling mechanism that could produce lower temperatures was attributed to the time delay of the optical pumping of atoms among these ground state sublevels. To counteract the optical pumping, and thereby sustain the cooling process, these models depend on optical polarization gradients to redistribute moving atoms among the sublevels of the ground state. The resulting damping force is much stronger and results in much lower final temperatures than Doppler cooling. How-

Figure 2.

The periodic potential derived from the light shift in a standing wave for two atomic sublevels that have different light shifts.

ever, this new mechanism is effective over a much narrower range of velocity.

The first optical molasses experiments[4] were done in three dimensions using three pairs of orthogonal, counterpropagating light beams. In this configuration polarization gradients can not be avoided, so both the Doppler and polarization gradient damping forces are simultaneously present. Thus atoms with speeds of up to a few times γ/k are "captured" by the Doppler molasses and slowed to velocities near the Doppler limit, $v_D = (\hbar\gamma/M)^{1/2}$. At this low speed the polarization gradient force with its strong damping can become effective, and rapidly cool the atoms toward much lower temperature.

Theory of Polarization Gradient Sub-Doppler Laser Cooling

The basic feature of the theory of polarization gradient sub-Doppler cooling derives from the spatial dependence of the light field in a standing wave.[10-12] Atomic energy levels can be shifted by the nearly resonant light, and this makes the internal atomic energy different in different parts of a standing wave. The result may be viewed as a spatially varying potential. For the case of a standing wave in one dimension, atoms move along a horizontal sinusoidal "washboard." For an atom with multiple ground states, the amplitude of the washboard may depend on which state it is in (see Figure 2).

In a standing wave tuned below atomic resonance, atoms at rest are optically pumped to the lowest sublevel of the ground state. For circularly polarized light, each scattering event (absorption followed by spontaneous emission) changes the magnetic quantum number by an integer ΔM, where $0 \leq \Delta M \leq 2$ for σ^+ (right circularly polarized) light, or by $-2 \leq \Delta M \leq 0$ for σ^- light. In each case, the selection rules dictate that atoms are pumped to the sublevel with an extreme value of M. Since this is also the sublevel that couples most strongly with the light, it is the most light-shifted and hence the lowest energy level as shown in Figure 3. A similar situation holds for linearly polarized light. In this case, the M = 0 sublevel is the one most strongly depressed by the light shift. When atoms are excited in a $\Delta M = 0$ process by the linear polarization, they may decay by $\Delta M = \pm 1$ or 0 transitions. Overall, decay toward M = 0 is favored, so atoms are again pumped toward this most light-shifted sublevel.

In a one-dimensional standing wave formed by counterpropagating beams of different polarizations, atoms moving parallel to the light beams encounter different polarizations along their paths. The quantization axis that defines the atoms' M sublevels (and hence the lowest level) is determined by the optical polarization. A particular angular momentum orientation (e.g., down) that corresponds to the lowest energy state at one point may correspond to a higher state at another point. Since moving atoms can not accommodate their orientations to that of the lowest level in a time less than the optical pumping time, their motion through the polarization gradient drives their lowest sublevel to higher energy. The resulting change in internal energy must occur at the expense of kinetic energy, and the atoms slow down. Thus the atomic motion results in the loss of mechanical energy as atoms travel through the standing wave because they are effectively moving up a hill. Optical pumping redistributes the populations among the ground state sublevels, but the time lag, or non-adiabaticity, results in the atoms' climbing up more than sliding down the hills. This "light shift" damping force is most effective for atomic speeds of $\lambda/2\pi$ per optical pumping time τ_p, corresponding to $v = \gamma_p/k$ where $\gamma_p \equiv 1/\tau_p$. We note that the Doppler effect plays no role in causing this force.

In addition to the velocity at which the force is most effective, another very important difference between velocity damping by the light shift force and by the Doppler force is

Figure 3.

Light shifts and the optical pumping scheme for Rb in σ^+ circularly polarized light.

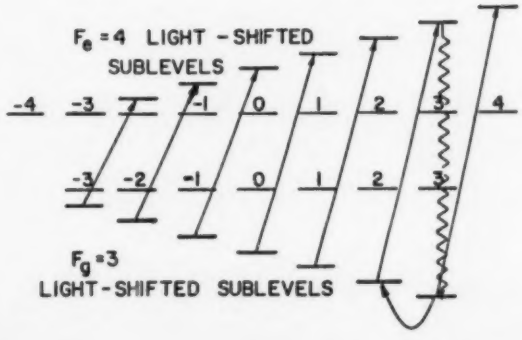

the effective velocity *range*. Both forces typically have about the same maximum strength, and both have a similarly shaped velocity dependence. (In Figure 1 γ need only be replaced by γ_p.) However, γ_p is generally much smaller than the excited state decay rate γ, making the effective velocity range of the light shift force γ_p/k much smaller than γ/k, the velocity capture range of the Doppler force. On the other hand, the damping constant is that much larger. Since heating from spontaneous emission is about the same in both cases, the final effective temperature is much smaller.

Affirmative tests of this model have recently been reported by the Paris group.[9] There are, however, some differences between their experiments and the model under test. In particular, the model is one dimensional but the experiments are done in a 3-D optical molasses. Secondly, the analytical results from the model apply only for simple optical transitions, but the experiments use a more complicated transition in Cs.

Stony Brook Theory and Experiments:

Subdoppler Cooling in a Magnetic Field

To test the model directly, the Stony Brook laser cooling group decided to build an experiment that mimicked the theoretical model as closely as possible. In the course of developing such a one dimensional test of the model, using optical collimation of an atomic beam, they discovered a *new* sub-Doppler laser cooling process. The group set out to do 1-D experiments both with and without polarization gradients. In the process they accidentally found that a weak magnetic field can do the job of the polarization gradient to achieve sub-Doppler temperatures.[8,13,14] A new theoretical model was then developed to describe these experiments. Moreover, it was found that adding a magnetic field to a light field that has a polarization gradient gives rise to new phenomena: deflection and simultaneous cooling of atoms to a non-zero velocity.[13,15,16] Incorporating this effect led to a very intuitive model using the concept of very narrow velocity selective resonances (VSR) to describe sub-Doppler laser cooling processes in general. The resonances enhance the redistribution of light between different beams of a standing wave, and can therefore yield a strong damping of the atoms to the resonance velocity.

The experiments use a thermal beam of natural Rb produced by an oven at T ≅ 150°C, with a horizontal slit aperture 0.1 mm high by 2 mm wide, and a vertical beam defining slit 0.1 mm wide by 2 mm high about 35 cm away (see Figure 4). The atoms emerge from the vertical slit in a horizontal fan-shaped beam and then interact with a pair of counterpropagating laser beams transverse to the atomic beam axis. The resulting atomic beam profile is measured with a scanning hot tungsten wire, 25 μm in diameter, 1.3 m away from the region of interaction with the laser beam. The laser light with $\lambda = 780$ nm is tuned near the $5S_{1/2}(F_g=3) \Rightarrow 5P_{3/2}(F_e = 4)$ cycling transition of ^{85}Rb. The laser and atomic beams cross perpendicularly, so the Doppler shifts are small. Atoms can only decay back to the $F_g = 3$ ground state; repumping them out of the $F_g = 2$ ground state is not needed. The laser frequency is calibrated with a saturated absorption signal from an auxiliary Rb cell at room temperature.

Figure 4.

Schematic diagram of apparatus.

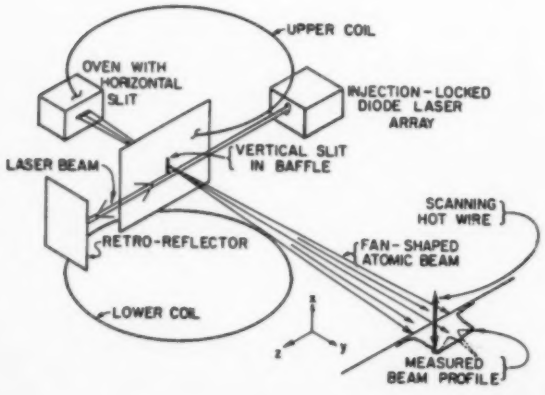

Figure 5.

Hot wire scan at two different magnetic field values showing spatial profile of laser cooled atomic beam. Here $s \equiv (\lambda^3\gamma/hc)I$ is a dimensionless intensity parameter that equals unity for $I = 4$ mW/cm^2 in Rb and δ is the laser detuning from atomic resonance. Note the difference in vertical scale for the two data sets.

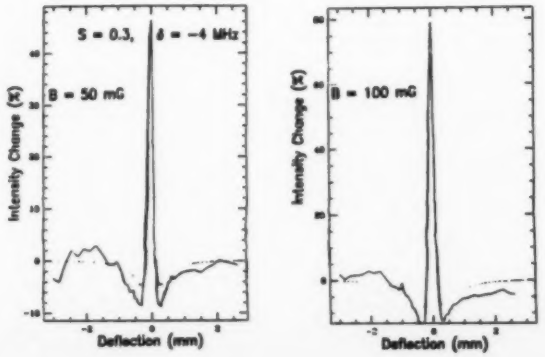

Low Field Experiments

These experiments occur in a B field as shown in Figure 4. A new cooling process was observed, resulting from the applied magnetic field instead of the polarization gradients, redistributing atoms among atomic ground state sublevels.[8,14] For small magnetic fields, the Stony Brook group observed narrow atomic velocity distributions centered at $v = 0$ with spreads as low as 2 cm/s in Rb (see Figure 5). This is much lower than the one dimensional Doppler limit $v_D = (7\hbar\gamma/20M)^{1/2}$ (= 10 cm/s, for Rb), where 7/20 is a geometrical factor.

Note that because these experiments use two counter-propagating laser beams that each have the *same* circular polarization, there is no polarization gradient. The main physical idea of this new cooling scheme, that is shared with that of Ref's. 10 and 11, is the different energy level shifts of the atoms' sublevels caused by the light. With the light tuned below resonance, these light shifts depress the ground state sublevels. Thus atoms near the peaks of the standing wave are optically pumped to the lowest sublevel (which is the highest M, as shown in Figure 3) because of the circular polarization. In this process, the atoms absorb light with lower frequency than they fluoresce, thereby losing internal energy.

To sustain the cooling process, atoms must be redistributed among the ground state sublevels, including the higher ones. This must be done near the nodes (zeros) of the standing wave where the light shifts are smallest. Redistributing by simply reversing the optical pumping process, however, would result in no net cooling. Instead, redistribution is accomplished by a weak magnetic field applied perpendicular to the laser beams as in Figure 4. The field induces transitions among the sublevels when an atom moves into a node where there is no light shift and no optical pumping. The levels are again degenerate, and mixing occurs by Larmor precession in the magnetic field without need of optical pumping. Also, at the nodes the atoms' internal energy increases because the negative light shift is smallest. This increase must come at the expense of kinetic energy (just as in Figure 2). Thus atoms having non-zero transverse velocity, i.e., having a component of velocity along the k vector of the standing wave, are optically pumped to the lowest energy sublevel near an antinode, and redistributed among the higher sublevels near a node. On the average, atoms climb higher hills than they descend, so travel across a series of antinodes extracts energy from the atoms, thereby damping their motion. This process is most effective when the optical pumping rate and the Larmor precession rate are comparable.

Figure 6.

The change in atomic beam profile of ^{85}Rb 1.3 m downstream from the molasses as measured by the hot wire for red (top) and blue (bottom) detuning. The laser parameters are $s = 0.25$, $\delta = \pm 0.67\gamma$ (see Figure 5 for definitions) and the magnetic fields are shown. The solid lines are experimental data and the dashed lines are the results from the theoretical model.

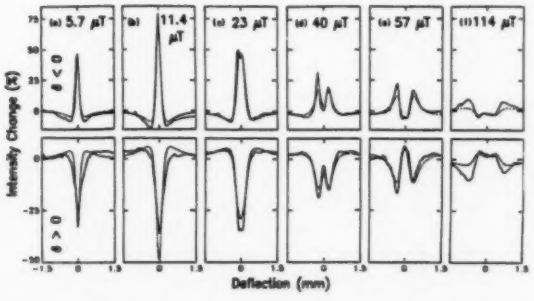

Figure 7.

The separation between the peaks for many data sets, including those of Figure 6, vs. magnetic field strength for the $F = 3 \Rightarrow 4$ transition in ^{85}Rb and the $F = 2 \Rightarrow 3$ transition in ^{87}Rb. Symbols denote experimental points for various intensities ($0.25 \le s \le 10$) and detunings ($1\gamma \le |\delta| \le 10\gamma$), using the average longitudinal velocity ($v \cong 350$ m/s) to convert the deflection angle into a transverse velocity. The solid lines are for the resonance condition.

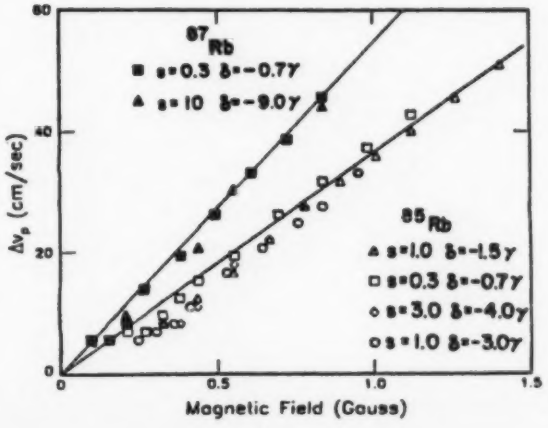

Figure 8.

Schematic diagram of atomic transitions at the resonance condition in VSR. The arrows do not exactly connect the levels because of the detuning of the laser d. The detuning can be quite large but is not relevant to the resonant condition for VSR. (a) shows the s+ - s- case where the ground state energies are split by a magnetic field. VSR between them requires the light frequencies to be different, and in the rest frame of a moving atom, this difference is provided by the Doppler shift. (b) shows the scheme for the lin⊥ lin *case (c) shows the case for v = 0 when a magnetic field is applied that splits the sublevels by more than* γ_p. *Different polarizations at different places cause either* $\Delta M_F = \pm 1$ *or* $\Delta M_F = 0$ *VSR.*

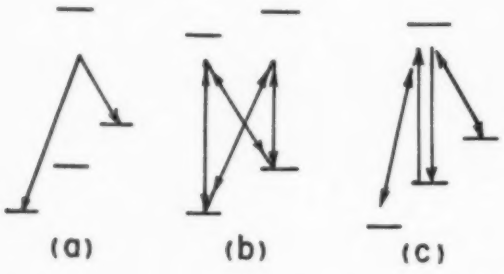

High Field Experiments

At larger magnetic fields, this picture involving optical pumping combined with Larmor precession breaks down: the precession becomes important even in the optical antinodes. In this high field case, the theory predicts that atoms will be cooled toward *two* finite velocities, symmetrically displaced from zero. Sub-Doppler cooling is still observed at large fields, but it occurs around non-zero velocities $\pm v_r$ that are proportional to the Zeeman splitting ω_z of the ground-state sublevels.[13,15,16] This results in the two peaks in the velocity distribution that can be seen in Figure 6. Since the velocities $\pm v_r$ are proportional to the Zeeman splitting the separation between these peaks is proportional to the applied magnetic field, as shown in Figure 7.

Velocity Selective Resonances

The double peak structure discussed above can be described in terms of momentum transfer by coherent two-photon transitions that induce velocity selective resonances (VSR) between two ground state sublevels. The VSR occur when the difference of the Doppler shifted frequencies of two light beams seen by a moving atom, $\mathbf{k}_1 - \mathbf{k}_2 \cdot \mathbf{v}$, equals the frequency splitting between a pair of ground state sublevels. Exciting new experiments have been done at Stony Brook in an applied uniform magnetic field **B**, with and without polarization gradients. Atomic beams can be both cooled and deflected or steered by the appropriate combinations of polarizations and magnetic field. The laser polarization and the direction of **B** in the VSR picture can be used to control the mean velocity to which atoms are cooled. It must be realized, however, that VSR alone is not sufficient to achieve sub-Doppler temperatures; there must also be dissipation, such as that provided by the non-adiabatic response of moving atoms to optical pumping in the changing light field.

To illustrate one of the simplest examples of VSR, consider a $\sigma^+ - \sigma^-$ polarization gradient scheme (i.e., counterpropagating σ^+ and σ^- beams) with an applied magnetic field **B** along the laser beam direction[16,17]. The σ^+ (σ^-) laser beam drives $\Delta M_F = +1$ (-1) transitions; the coherent two-photon process then couples ground state sublevels whose M_F values differ by ± 2 (see Figure 8a). Since $\mathbf{k}_1 = -\mathbf{k}_2$, the condition for VSR is then $2kv = \pm 2\omega_z$, where the sign depends on whether **B** is parallel to the σ^+ or the σ^- light beam.

VSR can also be created using optical molasses formed by two laser beams with orthogonal linear polarizations (called lin⊥ lin), and **B** perpendicular to the beams.[16] With **B**

Figure 9.

Change in the velocity selected beam profile of ^{85}Rb *1.3 m away from a* lin⊥ lin *optical molasses with* **B** *at 45° to both laser polarizations. The laser parameters are s = 3 and* $\delta = -18$ *MHz. (Remember that the data in Figure 6 was taken with no polarization gradient.)*

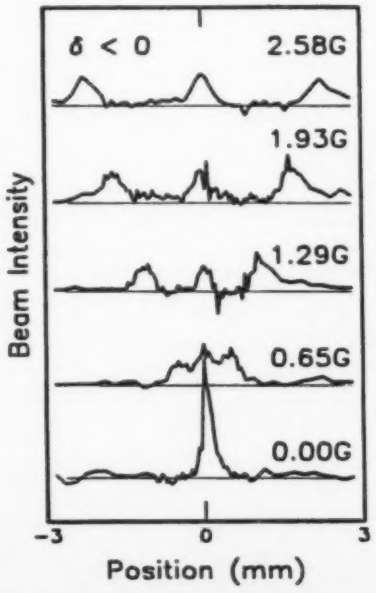

and the quantization axis parallel to the polarization of one laser beam, $\Delta M_F = 0$ transitions are induced, while the other beam induces $\Delta M_F = \pm 1$ transitions. In this configuration, VSR can couple ground state sublevels with M_F differing by ± 1; the VSR condition becomes $v = \omega_R/2k$, or one half that of the $\sigma^+ - \sigma^-$ case (see Figure 8b).

The VSR discussed so far are two-photon processes involving photons from two *different* laser beams that couple two different ground state sublevels (see Figures 8a,b). It is also possible to have sub-Doppler cooling in a strong **B** field involving two-photon processes that return an atom to its original ground state sublevel, while transferring a photon from one beam to another as before (central part of Figure 8c). This results in the resonant condition $v = 0$. This has been observed by applying **B** at 45° to both laser polarizations in the *lin* $\perp$ *lin* configuration.[16] This results in three cold peaks with sub-Doppler spread as shown in Figure 9. The center peak, which does not shift with **B**, corresponds to the $v = 0$ resonance shown in the center of Figure 8c, and the two side peaks correspond to the type of VSR shown in Figure 8b and on the sides of 8c. Numerical calculations corroborate all these results.[15]

Conclusions

It is now understood that the theory of sub-Doppler cooling processes can be unified under a description based on velocity selective resonances in a multi-level system. While a polarization gradient is necessary for some sub-Doppler cooling schemes, in other cases the state mixing is accomplished by having **B** along an axis different from the optically defined axis. As we have described, adding a magnetic field to laser cooling yields completely new phenomena.

There are many applications of cooling to non-zero velocities. If the deflection is applied to a previously decelerated beam, it is a superb method for extracting or steering a well defined cold beam. One could imagine building an atomic storage ring based on this deflecting and cooling technique. Such a stored beam would be ideal for precision spectroscopy, for the study of cold collisions and collective effects of cold atoms, and possibly in a new design for an atomic clock.

The VSR picture suggests extensions to more complicated systems. For example, sub-Doppler cooling could be realized in many atoms by VSR between two ground state hyperfine or fine structure sublevels where the VSR would be induced by two lasers tuned to *different* transitions. For example, for cooling Tl, one could use lasers at 378 nm and 535 nm to create VSR between the two ground state fine structure levels $6^2P_{3/2}$ and $6^2P_{1/2}$. Such two frequency laser cooling also results in the atoms being cooled to an appropriate resonance velocity. It is now possible to exploit technological progress to produce both of these wavelengths, respectively by frequency doubling a 756 nm diode laser and a diode pumped Nd^{+3} laser. Thus we have in principle a very attractive way to prepare high density, cold Tl atoms. These can be used, for example, for precision measurement of an atomic electric dipole moment. Such experiments are used to test fundamental symmetries such as time reversal invariance.

In conclusion, a unified description has been found for sub-Doppler cooling, and many applications have been suggested. Experiments currently being performed at Stony Brook, at N.I.S.T., and elsewhere will exploit these in the near future.

Biographies

Harold Metcalf is Professor of Physics at the State University of New York at Stony Brook and Director of Graduate Studies in Physics. He received his B.S. from the Massachusetts Institute of Technology and Ph.D. from Brown. His research interests include precision spectroscopy of simple atoms and molecules, quantum beats and atomic coherence, Zeeman spectroscopy, and laser cooling and trapping. He has been a visiting professor in Israel, France, China, and the Netherlands. He is a Fellow of the American Physical Society.

Peter Reynolds is a Program Manager at the Office of Naval Research in areas including atomic and molecular physics, clusters, chemical and computational physics. His undergraduate degree is from the University of California at Berkeley and his Ph.D. from the Massachusetts Institute of Technology. His research in critical phenomena in disordered systems, and in relating Monte Carlo and real space renormalization group methods, has become widely applied. More recently, his research has been on quantum simulations of atomic and molecular systems using ideas from statistical physics.

References

1. D. Wineland and H. Dehmelt, Bull. Am. Phys. Soc. **20**, 637 (1975).
2. T. Hansch and A. Schawlow, Opt. Commun. **13**, 68 (1975).
3. J. Dalibard and W. Phillips, Bull. Am. Phys. Soc. **30**, 748 (1985); W. Phillips et. al., J. Opt. Soc. Am. B **2**, 1751 (1985).
4. S. Chu et al., Phys. Rev. Lett. **55**, 48 (1985).
5. D. Wineland and W. Itano, Phys. Rev. A **20**, 1521 (1979).
6. P. Lett et. al., Phys. Rev. Lett. **61**, 169 (1988).
7. D. Weiss et. al., J. Opt. Soc. Am. B **6**, 2072 (1989).
8. B. Sheehy et.al., Phys. Rev. Lett. **64**, 858 (1990).
9. C. Salomon et. al., Europhys. Lett. **12**, 683 (1990).
10. J. Dalibard and C. Cohen-Tannoudji, J. Opt. Soc. Am. B **6**, 2023 (1989).

11. P. Ungar et. al., J. Opt. Soc. Am. B6, 2058 (1989).
12. C. Cohen-Tannoudji and W. Phillips, Phys. Today **43** 33 (1990).
13. S-Q. Shang et. al., Phys. Rev. Lett., **65**, 317 (1990).
14. B. Sheehy et. al., Chem. Phys. **145**, 317 (1990).
15. G. Nienhuis, P. van der Straten and S-Q. Shang, Phys. Rev. A **44**, 462 (1991).
16. S-Q. Shang et. al., Phys. Rev. Lett. **67**, 1094 (1991).
17. S-Q. Shang et. al., Atomic Physics 12, Ed. by J. Zorn and R. Lewis, World Scientific, 1991; see also abstracts of Twelfth I.C.A.P., postdeadline section in back of book.

Profiles in Science

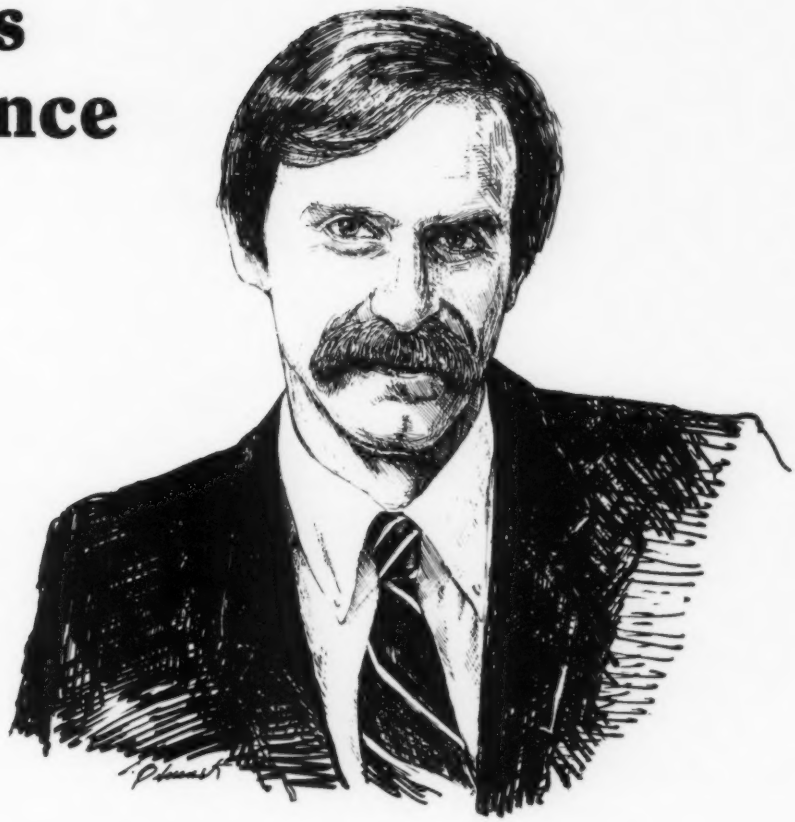

David J. Wineland

David J. Wineland, who is the leader of the Ion Storage Group at the National Institute of Standards and Technology (NIST), Boulder, Colorado, has been a principle investigator for the Office of Naval Research (ONR) over many years. A native of Milwaukee, Wisconsin, he received a bachelor's degree in physics from the University of California, Berkeley. Then from 1965 to 1970, he was a National Science Foundation Graduate Fellow at Harvard where he received M.A. and Ph.D. degrees while working on hydrogen and deuterium maser research under Norman Ramsey. For the next five years, he was a post-doctoral research associate at the University of Washington, Seattle, performing research with Hans Dehmelt on the rf spectroscopy of trapped electrons. Both of these mentors have since won the Nobel Prize for this and related work. In 1975, Wineland joined the Time and Frequency Division of the National Bureau of Standards (NBS) now NIST where his research group, with ONR funding, developed and applied laser cooling to trapped ions. This has led to experiments in high-resolution spectroscopy including the first atomic clock employing laser cooling. These techniques have also allowed experiments on such diverse topics as quantum measurements as well as liquid and solid plasmas. The article "Laser Cooling Atoms to Ultra-Low Temperatures in a Magnetic Field," which appears in this issue, describes an ONR research program closely related to Wineland's work.

The scientific community has recognized his achievements by making him a Fellow of the American Physical Society (APS), of the Optical Society of America (OSA), and of the National Bureau of Standards. In 1990, he received both the Davisson-Germer Prize of the APS and the William F. Meggers Award of the OSA.

Multispectral Image Enhancement Reveals Kuwaiti Oil Plumes

Thomas F. Lee and James Clark, Naval Research Laboratory
Maureen Thompson, Computer Sciences Corporation

Abstract

Absorbing of incoming solar radiation at visible wavelengths, oil smoke is nearly invisible over water on many environmental satellite images. To improve the detectability of smoke, the authors construct bispectral composites from images from the NOAA Advanced Very High Resolution Radiometer (AVHRR). These composites are constructed from a ratio between AVHRR channels 1 and 2. While neither channel by itself shows smoke over water, the ratio image often depicts smoke quite distinctly. The authors discuss an interactive program on a computer workstation which enables even an untrained user to develop further enhancements using this ratio image.

Introduction

The ongoing proliferation of satellite receiving workstations is revolutionizing environmental remote sensing. Just a few years ago, remote sensing display workstations were confined to large laboratories and major government installations. Data handling was often cumbersome and required large centralized data reception and distribution centers. Now satellite-receiving workstations are becoming more numerous and much more self-contained. These workstations allow image enhancement and manipulation in real time. As satellite workstations become more inexpensive, they are appearing all over the world in support of geology, oceanography, meteorology, hydrology and geography.

Relatively untrained scientists and technicians in the field are now trying to perform tasks which were once performed only by experts at central site facilities. Unfortunately, when operators do not know the basic principles of remote sensing and image enhancement, even the most powerful workstations can remain underutilized. Recognizing the vast potential of these workstations, the Naval Research Laboratory is designing interactive software packages that simplify the process of image enhancement. Once implemented in the field, our workstations will enable a large variety of analysts to arrive at useful products very quickly. We apply our techniques to smoke scenes from the recent Kuwaiti oil well fires in the Persian Gulf. Our data comes from the National Oceanic and Atmospheric Administration's (NOAA) polar-orbiting satellites.

Data

The Advanced Very High Resolution Radiometer (AVHRR) abroad the NOAA polar-orbiting spacecraft has proven to be a useful tool to study the Kuwaiti oil fires.[1] Its images come from five channels, representing five wavelength intervals. Channels 1 (.63 microns) and 2 (.86 microns) measure reflected solar radiation. Channel 3 (3.7 microns) measures both reflected solar (during the daytime) and emitted radiation. Channels 4 (10.8 microns) and 5 (11.8 microns) are located within the thermal infrared region. The AVHRR has 10-bit radiometric resolution which enables 1024 distinct gray levels. The NOAA satellites provide roughly twice-a-day coverage of a given region, yielding AVHRR "swaths" in a resolution of 1.1 km per pixel at nadir.

Background

The USS Wisconsin was stationed in the North Arabian Gulf when the smoke outbreak began. An after-action report by the Wisconsin[2] discussed the conditions encountered: "The smoke, caused by Iraqi forces igniting over 500 oil wells in Kuwait, produced an ominous overcast that completely blocked out the sun between 0900 to 1600 local (time), with ceilings from 0 to 300 feet. The ceilings encountered correlated well with a weak inversion layer noted on that days (sic) sounding. The smoke persisted for several days with the most severe being 03 Mar 91 when the sun was completely blocked bringing a night like darkness to the area. Horizontal visibility at the surface remained 2 to 4 nm using night vision equipment and the ship was able to continue low level helicopter operations."

Darkly-colored smoke, such as produced from the Kuwaiti oil fires, has attracted scientific attention for several years. Of all the potential atmospheric byproducts of nuclear war, black smoke has the greatest potential for altering the earth's climate ("nuclear winter" scenario). Crutzen et al. suggests that the light-absorbing smoke would block solar radiation, causing darkness and cold at the surface of the earth.[3] Thus, the burning oil wells in Kuwait became an "experiment of opportunity" for researchers modeling the effects of smoke on regional climate.[4,5]

Oil smoke differs from other kinds of smoke, for example forest fire smoke, due to its high soot content.[6,7] The high soot (elemental carbon) content explains its black color. Soot is produced only by actual combustion, as opposed to smoldering fires.[7] Viewed from above at visible wavelengths, the black appearance of oil smoke results from its high absorptivity (low reflectivity) and high optical depths.[8] Viewed from above at infrared wavelengths, oil smoke is semi-transparent. Thus, it tends to have a similar appearance to the image background.[1]

Figure 1.

NOAA AVHRR Channel 1 on 2 March 1991. Image is enhanced, but oil smoke is difficult to detect over the Persian gulf.

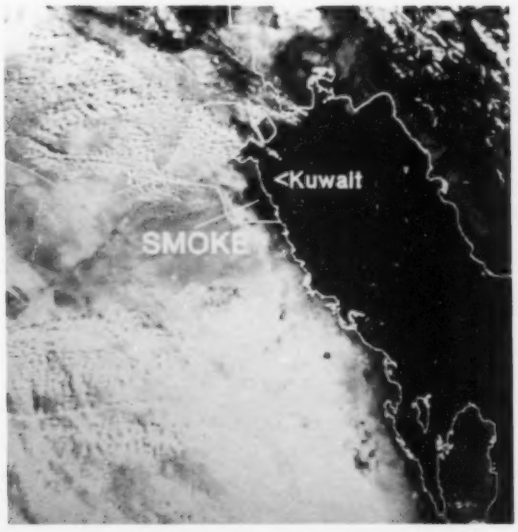

Figure 2.

NOAA AVHRR Channel 2 on 2 March 1991. As in channel 1 (Figure 1), oil smoke is not readily apparent.

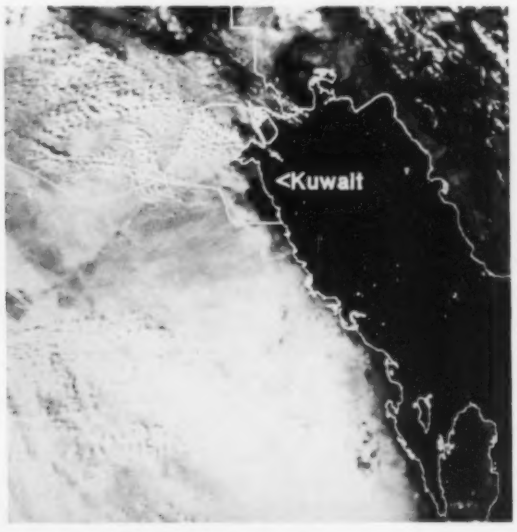

Case Study

On 2 March 1991 northwesterly winds blew oil smoke into the Persian Gulf. Channel 1 is "contrast-stretched" to enhance the lower (darker) reflectance values in the scene (Figure 1). On the image the northwestern tip of the smoke plume contrasts well over the bright Kuwaiti land background. However, despite the enhancement to show the darker regions of the scene, no smoke can be seen over the waters of the Persian Gulf. This lack of contrast appears because the smoke, like the underlying sea surface, reflects so little solar radiation. As in channel 1, an enhancement of channel 2 (Figure 2) shows no trace of oil smoke over the dark sea surface background.

Channel 3 (Figure 3) shows several white spots over Kuwait, representing the heat of several burning oil fields. These hotspots, which do not appear in the longwave infrared images (channels 4 and 5), are examples of the unique ability of channel 3 to detect tiny (much smaller than a 1 km pixel) but extremely hot features.[9,10,11,12] Channel 3 hotspots, which often appear just upwind of a smoke plume, are extremely useful in the identification of many smoke plumes. Over the sea surface, channel 3 gives a faint view of the smoke plume. The elevated smoke appears in dark grayshades, indicating a radiative temperature lower than the background. Channel 4 (Figure 4) and Channel 5 (not shown) show smoke faintly over the Persian Gulf near the Kuwaiti coastline. Away from shore the plume tends to blend with the sea surface in both channels.

Figure 5 shows a pixel-by-pixel ratio of channels 1 and 2. Compared to channels 1 and 2 (Figures 1-2) the ratio image shows improved detail over the Persian Gulf, but further enhancement is necessary to detect smoke. However, not all enhancements that could be applied are equally effective or appropriate. A preset (or "canned") enhancement, designed for repeated use with a particular product, often fails to deliver consistent results over a variety of scenes. A linear contrast stretch, which allows the analyst to establish appropriate high and low display limits, can produce a higher-quality enhancement than a preset enhancement. Unfortunately, a linear contrast stretch is time-consuming, requiring experimentation before arrival at a useful product.[13] Histogram equalization (described in Rees, 1990) increases the contrast over frequently occurring gray shades and decreases the contrast over infrequently occurring gray shades. It is not useful, however, to apply histogram equalization to Figure 5 because the area of Persian Gulf is small in relation to the image as a whole and contributes little weight to the histogram equalization procedure.

Our solution is to allow the analyst, using a mouse or a trackball, to select a small sub-area within the image as an area of interest (shown on Figure 5). Then, the program performs a histogram equalization on only the data values correspond-

Figure 3.

NOAA AVHRR Channel 3 on 2 March 1991. Hotspots (small bight areas over Kuwait) mark oil fires. Oil smoke plumes are moving downwind.

Figure 4.

NOAA AVHRR Channel 4 on 2 March 1991. Oil smoke plumes are difficult to detect downwind of Kuwait over the Persian Gulf.

ing to the subarea. Finally, it applies the resulting enhancement to the full area of the original image (Figure 6), revealing smoke plumes distinctly.

The ratio image (Figure 6) exploits the slightly different aerosol scattering properties of the shorter wavelength (channel 1) versus the slightly longer wavelength (channel 2).[14] In regions without smoke, channel 1 is more reflective than channel 2, suggesting significant channel 1 back-scattering by small, naturally occurring airborne aerosols. Where the sea is covered by oil smoke, on the other hand, the reflection received by the satellite is nearly identical in the two channels. The similarity results because smoke particles tend to be relatively large, favoring increased back-scattering at the longer wavelength. The ratio between the channels exploits these interchannel differences and produces an improved image over the Persian Gulf. Low values of the ratio (shown in bright gray shades on Figure 6) indicate smoke over the Persian. Gulf. High values (dark gray shades) indicate open water.

Discussion

Oil smoke produces fairly subtle signatures on satellite images, and no one AVHRR channel will always produce an easy-to-interpret image. The ratio image often produces dramatic improvement compared to individual channels, but even it will not always produce the optimal contrast between smoke and water. Thus, a user will often need to perform a series of enhancements. We have demonstrated an enhancement which can be performed quickly and without expertise, allowing unsophisticated analysts to arrive at useful products in a minimum of time. Such an approach is particularly valuable for field users under pressure to analyze imagery in a short period of time.

We have used the sub-area histogram equalization technique to enhance a ratio image, but the technique has broad applicability to a variety of images or image composites. This technique can also be applied to other phenomena besides oil smoke, In general, it is useful in the enhancement of any low-contrast feature which overs a small portion of an image. Ship and aircraft exhaust trails, urban heat islands, and fires are examples of phenomena which can be enhanced using this technique.

Acknowledgements

Dr. Philip Durkee, of the Naval Postgraduate School (Monterey, CA), gave valuable scientific suggestions. NOARL Contribution number 441:009:92. The authors gratefully acknowledge the support of the sponsor, the Office of

Figure 5.

Ratio image of channels 1 (Figure 1) and 2 (Figure 2). Small sub-area over the Persian Gulf shows region of histogram equalization for Figure 6.

Figure 6.

As in Figure 5, after sub-area histogram equalization.

Naval Technology, Code 22, Mr. James Cauffman, Program Element 62435N. Approved for public release; distribution is unlimited.

Biographies

Thomas Lee is a satellite meteorologist who has worked on the development of meteorological products for forecasters in the field. He has published papers on the detection of aircraft exhaust trails, the analysis of airborne dust, and the classification of extreme heat sources on the surface of the earth. At the present he is researching the capabilities of passive microwave sensors to analyze marine weather patterns.

James Clark is a satellite meteorologist who has worked extensively on the development of meteorological workstations. He helped to develop a prototype Navy workstation in the late 1970's (SPADS) and is now helping to develop the Navy Environmental Operational Nowcasting System (NEONS).

Maureen Thompson currently works for the Computer Science Corporation under contract to the Navy as the database manager for the NEONS relational data base system. She has worked on various government contracts after graduating with a B.S. in meteorology from San Jose State University.

References

1. Limaye, S.S., V.E. Suomi, C. Velden and G. Tripoli, 1991: Satellite observations of smoke from oil fires in Kuwait. *Science*, 252, 1536-1539
2. Commander, Naval Oceanography Command, 1991: USS Wisconsin (BB64) Post Deployment Report, (Enclosure 1) 09 August 90-28 March 1991. Navoceancom Report 3140-5, Stennis Space Flight Center, MS 39529-5000.
3. Crutzen, P.J., I.E. Galbally and C. Bruhl, 1984: Atmospheric effects of post-nuclear fires. *Climatic Change*, 6, 323-364.
4. Browning, K.A., R.J. Allam, S.P. Ballard, R.T.H. Barnes, D.A. Bennetts, R.H. Maryon, P.J. Mason, D. McKenna, J.F.B. Mitchell, C.A. Senior, A. Slingo and F.B. Smith, 1991: Environmental effects from buring oil wells in Kuwait. *Nature*, 351, 363-367.
5. Bakan, S., A. Chlond, U.Cubasch, J. Feichter, H. Fraf, H. Grassl, K. Hasselmann, I. Kirchner, M. Latif, E. Roeckner, R. Sausen, U. Schlese, D. Schriever, I. Schult, U. Schumann, F. Sielmann and W. Welke, 1991: Climate response to smoke from the buring oil wells in Kuwait. *Nature*, 351, 367-371.
6. Chung, Y.S., and H.V. Le, 1984: Detection of forest-fire smoke plumes by satellite imagery. *Atmos. Envir.*, 18, 2143-2151.
7. De Vries, P.J., 1989: Analysis of forest fire smoke using satellite imagery. Masters thesis, Naval Postgraduate School, Meteorology Department, Monterey CA 93943-5000, 71 pp.
8. Pittock, A.B., T.P. Ackerman, P.J. Crutzen, M.C. MacCracken, C. S. Shapiro and R.P. Turco, 1986: *Environmental Consequences of Nuclear War, Volume I Physical and Atmospheric Effects.*, John Wiley and Sons, 358 pp.
9. Dozier, J., 1981: A method for satellite identification of surface temperature fields of subpixel resolution. *Remote Sensing Environ.*, 11, 221-229.
10. Matson, M., and J. Dozier, 1981: Identification of subresolution high temperature sources using a thermal IR sensor. *Photogrammetric Engineering and Remote Sensing*, 47, 1312-1318.
11. Lee, T.F., and P.M. Tag, 1990: Improved Detection of Hotspots using the AVHRR 3.7 um channel. *Bull. Amer. Meteor. Soc.*, 71, 1722-1730.
12. Robinson, J.M., 1991: Fire from space: Global fire evaluation using infrared remote sensing. *Int. J. Remote Sensing*, 12, 3-24.
13. Rees, W.G., 1990: *Physical Principles of Remote Sensing*, Cambridge University Press, 247 pp.
14. Haggerty, J.A., P.A. Durkee and B.J. Wattle, 1990: A comparison of surface and satellite-derived aerosol measurements in the western Mediterranean. *J. Geophys. Res.*, 95 (C2), 1547-1557.

Thermoacoustic Refrigeration for Space Applications

Steven L. Garrett, Jay A. Adeff, and Thomas J. Hofler
Naval Postgraduate School

Abstract

A new spacecraft cryocooler which uses resonant high amplitude sound waves in inert gases to pump heat will be described. The phasing of the thermoacoustic cycle is provided by thermal conduction. This "natural" phasing allows an entire refrigerator to operate with only one moving part (the loudspeaker diaphragm). A space-qualified thermoacoustic refrigerator designed and fabricated at the Naval Postgraduate School was flown as a Get Away Special (NASA G-337) on Space Shuttle *Discovery* (STS-42) in January, 1992. It was entirely autonomous, had no sliding seals, required no lubrication, used mostly low-tolerance machined parts, and contained no expensive components. Because the compressor's moving mass was small (≈ 15 gm) and its oscillation frequency is high (≈ 400 Hz), the vibrations were insignificant. This low vibration and lack of sliding seals makes thermoacoustic refrigeration an excellent candidate for small satellite applications. Since thermoacoustic refrigerators use no CFC's and have coefficients-of-performance which are competitive with conventional vapor compression (Rankine) cycle refrigerators, thermoacoustics is also a good candidate for food refrigerator/freezers and commercial/residential air conditioners. The design and performance of the Space ThermoAcoustic Refrigerator (STAR) will be described and other thermoacoustic research currently in progress at NPS will be presented.

Introduction

The ubiquity of reliable and inexpensive refrigerators, freezers, and air conditioners in our daily experience produces a general complacency with regard to cooling engines that is responsible for some unpleasant consequences in both commercial and military applications. Recent ratification of the Montreal Protocols, an international agreement to ban the worldwide production of chlorofluorocarbons (CFCs)[1], and the failure of the chemical companies to produce stable, nontoxic, energy efficient, and environmentally safe CFC replacements for Rankine cycle coolers[2], could have significant economic and social consequences.

One of the most obvious military problems generated by "refrigeration complacency" is the failure to develop reliable spacecraft cryocoolers with low vibration levels for use with infrared imaging. A manifestation of this bias against advanced refrigeration research and development was the cre-

ation, at great expense, of the sensors to be used by the Strategic Defense Initiative Organization (SDIO), all of which require active cooling, without a parallel development program for long-life, low vibration, space-based cryocoolers. The discovery of Hi-T_c superconductors, which may find use in high speed electronics and signal conditioners, SQUID sensors, and computers, will only compound the military problems generated by this lack of inexpensive, long-lived, and compact cryocooler technology.

Since 1986, the Naval Postgraduate School has been attempting to alter this situation by an extensive research and development program based on the recently discovered[3] thermoacoustic heat pumping cycle. These efforts have included basic research into the nonlinear acoustics of both the thermoacoustic heat pumping process[4] and the generation of high amplitude sound by temperature gradients[5,6], as well as the development of an autonomous, space-qualified thermoacoustic refrigerator.

The Space ThermoAcoustic Refrigerator was launched as a Get Away Special on the Space Shuttle *Discovery* (STS-42) in January, 1992, and will be the focus of this article. Before presenting a description of its most unique sub-systems, we will present a simplified discussion of the principles of thermoacoustic refrigeration.

The Thermoacoustic Heat Pumping Cycle

The interaction between acoustics and thermodynamics has been recognized ever since the dispute between Newton and Laplace over whether the speed of sound was determined by the adiabatic or isothermal compressibility of air. Although today there are probably many physicists who might still make the wrong choice (as Newton did!), most physicists have at least been exposed to a lecture demonstration such as the Rijke Tube[7] or have cursed Taconis oscillations in liquid helium[8], so they are not surprised that temperature gradients can lead to the production of sound. The reverse process – thermoacoustic heat pumping – is far less well known and was the first intentional demonstration of a new class of intrinsically irreversible heat engines.

Traditional heat engine cycles, such as the Carnot Cycle typically studied in elementary thermodynamics courses, assume that the individual steps in the cycle can be made reversibly. Such analyses, which invoke the First and Second Laws of Thermodynamics, lead to the limiting values for the efficiencies of prime movers and the coefficients-of-performance of refrigerators. These limiting values are never realized in practical heat engines and refrigerators due to the unavoidable irreversibilities, such as thermal diffusion, the pressure dependance of the thermophysical properties of real working fluids, and viscous dissipation, which always reduce performance below the ideal Carnot values. Reversible engines also require various mechanical devices (eg. valves, cams, push-rods, linkages, timing chains, etc.) in order to execute the proper phasing of various cyclic processes (eg. compressions, expansions, displacements, regeneration, etc.). In thermoacoustic engines, the irreversibility due to the imperfect (diffusive) thermal contact between the acoustically oscillating working fluid and a stationary second thermodynamic medium (the "stack") provides the required phasing. This "natural phasing" has produced heat engines which require no moving parts other than the self-maintained oscillations of the working fluid.

A Simple, Invisid, Lagrangian Model of the Heat Pumping Process

Although a complete and detailed analysis of the thermoacoustic heat pumping process is well beyond the scope of this article, the following simple, invisid, Lagrangian representation of the cycle contains the essence of the process. A complete analysis[9] would necessarily include the gas viscosity, finite wavelength effects, longitudinal thermal conduction along the stationary second thermodynamic medium and through the oscillating gas, and the ratios of the heat capacities of the gas and second medium.

Figure 1.

Schematic diagram of a one-quarter wavelength thermoacoustic refrigerator shown in cross-section. The loudspeaker at the left sets up the standing wave in a gas-filled tube. The termination at the right-hand end of the tube is rigid. To the left of the termination is a stack of plates (the "stack") whose spacing is chosen to be a few thermal penetration depths. Below the resonator is a expanded view of a portion of the stack and a parcel of gas undergoing an acoustic oscillation.

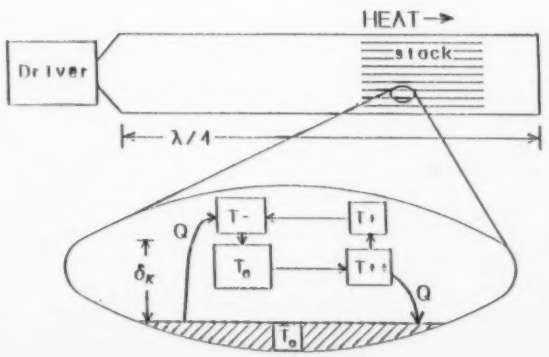

A schematic diagram of a simple, one-quarter wavelength, $\lambda/4$, thermoacoustic refrigerator is shown in Figure 1. The loudspeaker at the left maintains the standing wave within the gas-filled tube. Its frequency is chosen so that the loudspeaker excites the fundamental ($\lambda/4$) resonance of the tube.

Figure 2.

Lagrangian, invisid picture of the thermoacoustic heat pumping cycle. In the first step the gas parcel is adiabatically compressed and its temperature is raised above that of the plate. During the second step the hot parcel rejects some of its heat to the plate and lowers its temperature. The third step is the reverse of the first but since the adiabatic expansion starts from a lower temperature it ends at a lower temperature. During the final step the parcel which is cooler than the plate adsorbs heat from the plate thereby cooling the plate and warming itself. The net effect is to absorb work from the sound field and pump heat up a temperature gradient. The parcels act as a "bucket brigade", picking up heat at the left (lower temperature) and handing it off to the next parcel at the right (higher temperature).

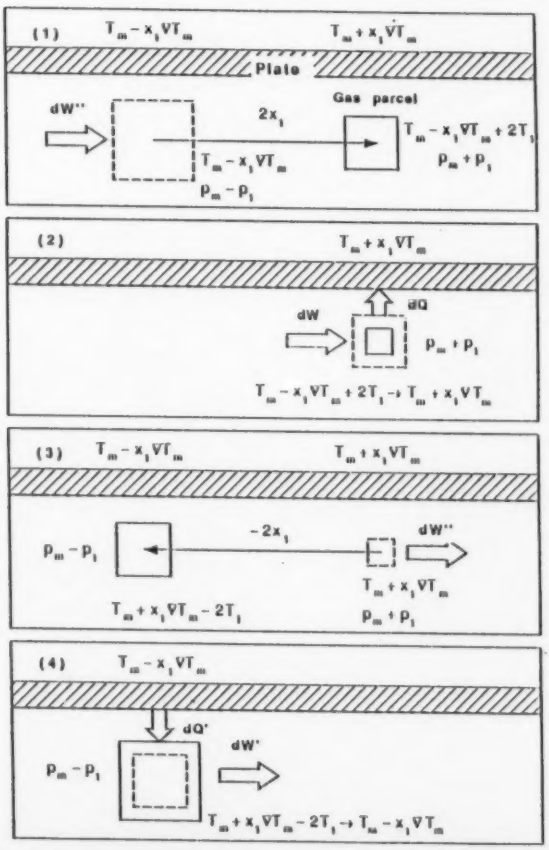

The termination at the right-hand end of the tube is rigid so the longitudinal particle velocity at that end is zero (a velocity node) and the acoustical pressure variations are maximum (a pressure antinode). We have arbitrarily assumed that the loudspeaker is "ultracompliant"[10], so that the left end of the tube is an acoustic pressure node and a particle velocity antinode. (If the loudspeaker was assumed to be noncompliant then the tube would be a half-wavelength long.) To the left of the rigid termination is a stack of plates (the "stack") whose spacing is chosen to be a few thermal penetration depths.

The thermal penetration depth, δ_κ, represents the distance over which heat will diffuse during a time which is on the order of an acoustic period, $T = 1/f$, where f is the acoustic frequency. It is defined[11] in terms of the thermal conductivity of the gas, κ, the gas density, ρ, and its isobaric specific heat (per unit mass), c_p.

$$\delta_\kappa = \sqrt{\frac{\kappa}{\pi f \rho c_p}} \qquad (1)$$

This length scale is crucial to understanding the performance of the thermoacoustic cycle since the diffusive heat transport between the gas and the "stack" is only significant within this region. It is for that reason that the stack and the spacing between its plates are central to the thermoacoustic cycle.

For this analysis we will focus our attention on a small portion of the "stack" and the adjacent gas which is undergoing acoustic oscillations at a distance from the solid stack material which is small enough that a substantial amount of thermal conduction can take place in an amount of time which is on the order of the acoustic period. In the lower half of Figure 1, a small portion of the stack has been magnified and a parcel of gas undergoing an acoustic oscillation is shown schematically. The four steps in the cycle are represented by the four boxes which are shown as moving in a rectangular path for clarity although in reality, of course, they simply oscillate back and forth[12]. As the fluid oscillates back and forth along the plate it undergoes changes in temperature due to the adiabatic compression and expansion resulting from the pressure variations which accompany the standing sound wave. The compressions and expansions of the gas which constitute the sound wave are adiabatic if they occur farther than a few δ_κ from the surface of the plate. The relation between the change in gas pressure due to the sound wave, p_1, relative to the mean (ambient) pressure, p_m, and the adiabatic temperature change of the gas, T_1, due to the acoustic pressure change, relative to the mean absolute (Kelvin) temperature, T_m, is derived from the adiabatic equation of state for an ideal gas and is given below in equation (2).

$$\frac{T_1}{T_m} = \frac{\gamma - 1}{\gamma}\frac{p_1}{p_m} \qquad (2)$$

The polytropic coefficient, γ, is equal to the ratio of the specific heat of the gas at constant pressure to the specific heat at

Figure 3.

Scale drawing of STAR in its GAS canister. The canister inside diameter is 20.00" (508 mm) and the distance from the bottom of the lid to the bottom of the lower battery box is 28.25" (718 mm). The thermoacoustic engine is surrounded by a vacuum can which provides thermal insulation and vents to space through the lid. Behind the vacuum can is the gas ballast volume (1 liter). Not shown are the two electronics enclosures and the switching power amplifier. Its total weight excluding the canister is one pound less than the GAS limit of 200 lbs (90.7 kg.).

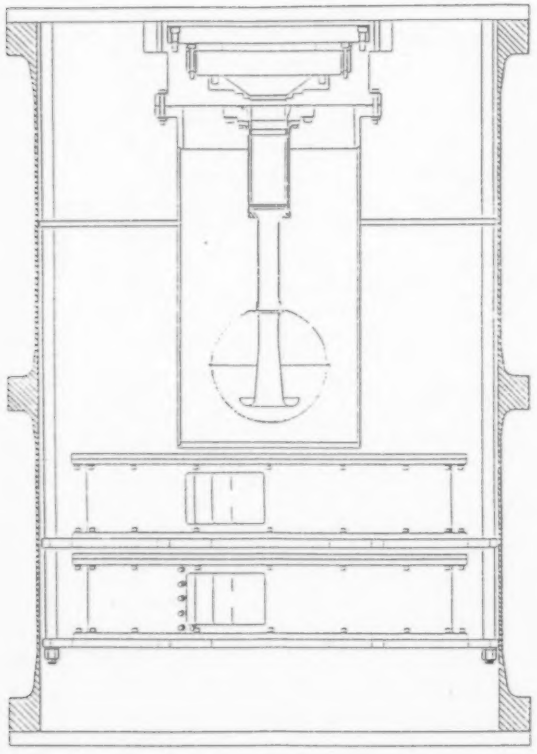

constant volume and is exactly 5/3 for the inert gases at the pressures of interest. It is smaller for all other gases but is always greater than one.

Although the oscillations in an acoustic heat pump are sinusoidal functions of time, Figure 2 depicts the motion as articulated (a square wave) in order to simplify the explanation. The thermodynamic cycle can be considered as consisting of two reversible adiabatic steps and two irreversible isobaric (constant pressure) steps. The plate is assumed to have a mean temperature, T_m, and a temperature gradient, ∇T, referenced to the mean position, $x = 0$. The temperature of the plate at the left-most position of the gas parcel's excursion is therefore $T_m - x_1 \nabla T$, and at the right-most excursion is $T_m + x_1 \nabla T$.

In the first step of this four-step cycle, the fluid is transported along the plate by a distance $2x_1$ (the peak-to-peak displacement) and is heated by adiabatic compression from a temperature of $T_m - x_1 \nabla T$ to $T_m - x_1 \nabla T + 2T_1$. The adiabatic gas law provides the relationship between the change in gas pressure, p_1, and the associated change in temperature, T_1, as described in equation (2). Since we are considering a heat pump, $2T_1 > 2x_1 \nabla T$, and work, in the form of sound, is done on the gas parcel. The gas parcel is therefore at a temperature which is higher than that of the plate at its present location.

In the second step, the warmer gas parcel transfers an amount of heat, dQ_{hot}, to the plate by thermal conduction at constant pressure and its temperature decreases to that of the plate, $T_m + x_1 \nabla T$. In the third step, the fluid is transported back along the plate to position $-x_1$ and is cooled by adiabatic expansion to a temperature $T_m + x_1 \nabla T - 2T_1$. This temperature is lower than the original temperature at location $-x_1$, so in the fourth step the gas parcel adsorbs an amount of heat, dQ_{cold}, from the plate thereby raising its temperature back to its original value, $T_m - x_1 \nabla T$.

The net effect of this process is that the system has completed a cycle which has returned it to its original state and an amount of heat, dQ_{cold}, has been transported up a temperature gradient by work done in the form of sound. It should be re-emphasized again at this point that no mechanical devices were used to provide the proper phasing between the mechanical motion of the gas parcel and the thermal effects.

If we now consider the full length of the stack as shown in the upper portion of Figure 1, the overall heat pumping process is analogous to a "bucket brigade" in which each set of gas parcels picks up heat from its neighbor to the left at a lower temperature and hands off the heat to its neighbor to the right at a higher temperature. Heat exchangers are placed at the ends of the stack to absorb the useful heat load at the left-hand (cold) end of the stack and exhaust the heat plus work (enthalpy) at the right-hand (hot) end of the stack. The fact that the individual gas parcels actually move a distance which has typically been on the order of several millimeters means that good physical contact between the heat exchangers and the stack is not crucial since the moving gas can provide the requisite thermal contact.

Thermoacoustic Energy Transport

If there were no external (*i.e.*, useful!) heat load applied to the stack and no longitudinal heat conduction along the stack, then eventually the temperature gradient in the plate would approach that caused by the adiabatic processes in the gas. In the absence of gas viscosity, this critical temperature gradient, ∇T_{crit}, is a function only of the gas thermophysical

Figure 4.

Scale drawing of the STAR acoustical sub-systems showing the driver, resonator, stack, and heat exchangers in cross-section.

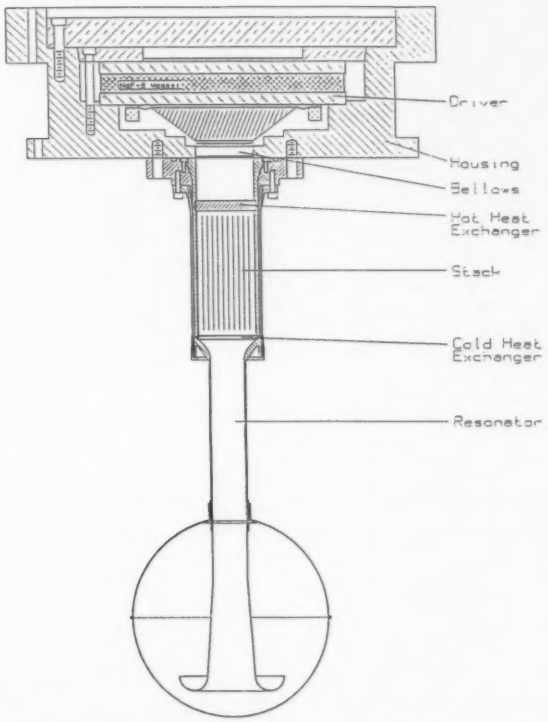

properties, the wavelength of the sound, λ, and the mean position of the stack, x, within the standing wave field.

$$\nabla T_{crit} = \frac{2\pi(\gamma-1)}{\lambda}\tan\left(\frac{2\pi x}{\lambda}\right) \qquad (3)$$

The ratio between the temperature gradient in the stack and the critical gradient, $\Gamma = \nabla T_m/\nabla T_{crit}$, plays an important role in the performance of the stack as will be explained below.

The rate of heat transport or heat pumping power, Q_2, within the stack can be expressed in a simple form if we assume that the stack is much shorter than the wavelength of the sound and we again neglect viscosity.

$$Q_2 = -\frac{\Pi\delta_\kappa}{4} p_1 u_1 (\Gamma - 1) \qquad (4)$$

The prefactor in (4) is simply one quarter of the thermally effective cross-sectional area of the stack, where Π is the stack perimeter and δ_κ is again the thermal penetration depth. The heat pumping power is also proportional to the product of the acoustic pressure, p_1, and the acoustic particle velocity, u_1, within the stack. If the stack were located at a pressure or velocity node, no heat pumping would take place since either the pressure variations which cause the adiabatic temperature changes would be absent or there would be no motion of the gas parcels. Since pressure and particle velocity are proportional (the proportionality constant depends upon the location of the stack within the standing wave field), a doubling of the acoustic pressure would quadruple the heat transport. This is the origin of the subscript "2" on the heat transport symbol, Q_2, which emphasizes the fact that the magnitude of the thermoacoustic heat transport depends upon the square of the linear acoustic field variable.

The parenthetical factor in equation (4) is a measure of how close the system is to the limiting temperature gradient. As mentioned before, when $\Gamma = 1$, the gas parcels "see" their adiabatic temperature span on the stack so no heat transfer from the gas to the plate takes place. When $\Gamma = 0$, the temperature of the plate is uniform and the greatest quantity of heat is pumped by the oscillating gas parcels.

The stack also absorbs work, W_2, at a rate proportional to $(\Gamma - 1)$. The following simple expression for the work absorbed by the stack of length Δx, in the absence of viscosity, can be written if one assumes that the heat capacity of the stack is much greater than that of the gas.

$$W_2 = \frac{\Pi\delta_\kappa}{4}\nabla x\frac{(\gamma-1)}{\gamma p_m} 2\pi f (p_1)^2 (\Gamma - 1) \qquad (5)$$

This work represents the acoustical energy dissipated due to irreversible thermal conduction between the gas and the plate.

The ratio of the heat pumped, Q_2, to the work done, W_2, to pump that heat, is defined as the coefficient-of-performance (COP) of the refrigerator. Since the temperature which is spanned by the stack is $\Delta T = \Gamma\nabla T_{crit}\Delta x$, one can show that the thermoacoustic COP = Γ COP_{Carnot}, where $COP_{Carnot} = T_{Cold}/\Delta T$. The Carnot coefficient-of-performance is dictated by the First and Second Laws of Thermodynamics. Since for a heat pump, $\Gamma < 1$, we see that the thermoacoustic COP is always less than that of Carnot. We also see that with the thermoacoustic heat pump, there will be the same competition between power density and efficiency which exists in all heat engines. As we pointed out earlier, there is no useful heat pumped when $\Gamma = 1$, which is the point where the efficiency is at its maximum and when $\Gamma = 0$, the heat pumping is greatest and the COP = 0.

The general results derived above from the simple, invisid picture are essentially preserved when the viscosity of the gas is included but the detailed mathematical descriptions are substantially more complicated. Even under the simplest assumptions regarding stack length, Δx, the Prandtl Number, σ, the viscous penetration depth, δ_v, and the ratio of the stack half-spacing to the viscous penetration depth, δ_v/y_o, the equa-

tions for enthalpy and work which are the equivalent of equations (4) and (5) become (6) and (7) written below:

$$H_2 = \frac{-\Pi\delta_\kappa}{4} \frac{T_m \beta p_1^2 (u_1^2)}{(1+\delta)(1+\varepsilon_s)(1-\delta_v/y_o+\delta_v^2/2y_o^2)}$$

$$\times \left[\Gamma \frac{1+\sqrt{\sigma}+\sigma+\sigma\varepsilon_s}{1+\sqrt{\sigma}} - (1+\sqrt{\sigma}-\delta_v/y_o)\right]$$

$$- \Pi (y_o K + 1 K_s) \frac{dT_m}{dx} \qquad (6)$$

$$W_2 = \frac{-\Pi\delta_\kappa \Delta x}{4} \frac{\omega(\gamma-1)(p_1)^2}{\rho_m a^2 (1+\varepsilon_s)}$$

$$\times \left[\frac{\Gamma}{(1+\sqrt{\sigma})(1-\delta_v/y_o+\delta_v^2/2y_o^2}-1\right]$$

$$- \frac{\Pi\delta_v \Delta x}{4} \frac{\omega\rho_m <u_1>^2}{(1-\delta_v/y_o+\delta_v^2/2y_o^2)} \qquad (7)$$

Discussion of these equations, as well as strategies for their optimization, is well beyond the scope of this brief introduction to thermoacoustics. The reader is referred to the excellent review article by Swift[9] for a detailed derivation and discussion of these more complete results.

The Space Thermoacoustic Refrigerator (STAR)

STAR was the first attempt to demonstrate the advantages of the thermoacoustic heat pumping cycle for cryocooler applications in space. It is intended to operate autonomously in low Earth orbit aboard the Space Shuttle in a Get Away Special (GAS) canister shown in Figure 3. It derives its power from an internal battery power source (700 Watt-hours) and was optimized for a modest temperature span ($\Delta T \leq 80^\circ$ K) and small heat loads ($Q_{cold} \leq 5$ Watts). Due to requirements of small size and light weight imposed by the GAS envelope, it operates at a frequency of about 400 Hz and is driven by an electrodynamic loudspeaker.[13] Its frequency of operation is adjusted automatically[14] to keep the system on resonance. The resonator length is approximately equal to a quarter wavelength of sound in a mixture of helium and argon or helium and xenon gas[15] maintained at a mean pressure of ten atmospheres (1.0 MPa). It has a single stack with a uniform spacing. The stack is fabricated by gluing fishing line to polyester film (Mylar™) and rolling the film up like a "jelly roll".[15,16] The stack used in STAR is 7.9 cm in length and 3.8 cm in diameter. Copper-fin, parallel plate heat exchangers are located at either end of the stack. Figure 4 is a scale drawing of the acoustical sub-systems.

Acoustical Sub-Systems.

The driver housing does more than simply hold the electrodynamic driver. The considerable mass and size of the housing is a consequence of the fact that a commercially available loudspeaker was modified for this application. The driver housing serves as a heat sink for the heat generated by the resistive losses in the driver voice coil and the heat pumped away from the cold end of the resonator. It also contains the ten atmospheres of the helium/xenon gas mixture which is the "working fluid" within the refrigerator. The housing is bolted to the standard 12 inch bolt circle provided on the GAS canister lid which acts as the radiator while on orbit.

The driver voice coil is attached to an aluminum reducer cone which is in turn bonded to an electroformed nickel bellows. The bellows provides a means of transferring acoustic pressure to the resonator without the need for sliding seals. A miniature accelerometer is attached to the surface of the reducer cone opposite the bellows to monitor the displacement magnitude and its phase relative to the acoustic pressure at the face of the bellows. That acoustic pressure is monitored by a piezoelectric quartz microphone[17] followed by a MOSFET impedance converter located within the driver housing in close proximity to the microphone.

A capillary leak is provided between the driver housing internal volume and the resonator to allow for pressure equalization during operation and for the purging and filling of the entire system through a single port located at the side of the driver housing. There are electrical feed-thrus to provide access to the driver voice coil, microphone, and accelerometer. Finally, there is a piezoresistive pressure gauge mounted to the side of the housing to monitor the mean pressure of the gas mixture.

The resonator is a modified quarter wavelength tube. The open end is terminated by a tapered "trumpet" and sealed by a surrounding sphere. Thus, an "open" termination is simulated while still allowing the resonator to retain the ten atmospheres of gas mixture. The thermoacoustic stack and heat exchangers are located in a section of the resonator designed to reduce heat conduction back to the cold end. The resonator is instrumented with semiconductor diode thermometers at both the cold and hot ends and is wrapped with multiple layers of superinsulation (aluminized Mylar™ and fiberglass) to prevent heating by thermal radiation. An electrical strip heater element is attached to the cold end of the resonator near the cold heat exchanger to permit measurement of refrigerator performance with a variable and quantifiable heat load. A thermal isolation vacuum chamber surrounds the resonator and seals against the bottom surface of the driver housing with an O-ring.

Electrical Sub-Systems.

In order for the refrigerator to operate autonomously in space, a family of analog and digital electronic circuits are employed to monitor the "health" of the system, keep the driver running at the proper amplitude and frequency, and to acquire and store useful data for post-flight analysis. The design and function of each of these electronic sub-systems is documented in Reference 14.

The circuit which is unique to this application is the Resonance Control Board (RCB). Its function is to maintain the system at acoustical resonance and to control the amplitude of the acoustical pressure at pre-determined levels dictated by the Controller Board. The speed of sound, a, and hence the resonance frequency of the refrigerator, is a function of temperature.

$$a = \left(\frac{\partial p}{\partial \rho}\right)_s^{\frac{1}{2}} = \sqrt{\frac{\gamma RT}{M}} \qquad (8)$$

In equation (8), γ is again the polytropic coefficient, M is the mean molecular weight of the gas mixture, and R is the universal gas constant. As the temperature changes, the sound speed changes, hence, for fixed resonator dimensions, the resonance frequency will be a function of temperature.

It is important that the system be maintained at resonance for two reasons. The first is that the resonance enhances the acoustic pressure generated within the resonator for a given velocity of the bellows. This resonant enhancement of the pressure is partially responsible for the fact that no sliding seals are required in the system since only small driver excursions are required to produce the necessary acoustical levels. The second reason for maintenance of the system on acoustic resonance is more subtle but equally important. The values of the temperature span produced by the refrigerator and its heat pumping capacity are a strong function of the position of the stack with respect to the standing sound wave as demonstrated by equations (3) through (5). For a particular application, this stack position must remain fixed. Since the stack is not movable, the wavelength of the sound must remain constant, hence, the frequency of the sound must be varied in order to compensate for the changes in the sound speed with temperature described in equation (8).

The RCB maintains the resonance condition by comparing the relative phase of the microphone and accelerometer outputs. At resonance the pressure and velocity of the gas mixture at the bellows location must be in-phase. Therefore, the pressure and acceleration are required to be in quadrature (*i.e.*, 90° out-of-phase). The two signals are electronically multiplied together and the dc-component of their product, which is proportional to the cosine of their phase difference, is used as an error voltage. This error voltage is electronically integrated and fed back to a voltage controlled oscillator to close the phase-locked-loop circuit which maintains the entire system at resonance.

The acoustical amplitude is controlled by a similar feedback circuit within the RCB which compares the microphone

Figure 5.

The ratio of the cold and hot heat exchanger temperatures, T_c/T_h, as a function of heat load on the cold heat exchanger at an acoustic pressure ratio of p_1/p_m = 2% in a lean mixture (4% Xe) of helium and xenon.

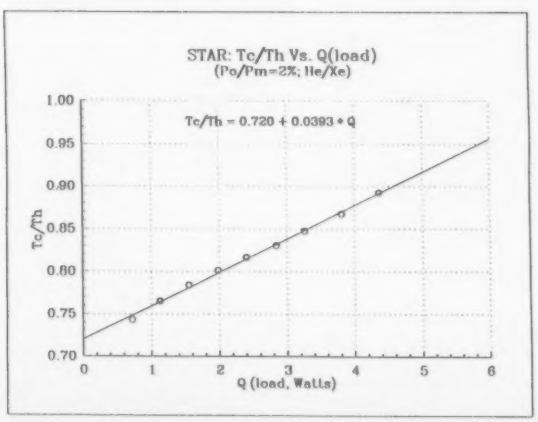

Figure 6.

Measured coefficient-of-performance relative to the ideal Carnot coefficient-of-performance (COPR) as a function of heat load for STAR operating at an acoustic pressure ratio of p_1/p_m = 2% in a lean mixture (4% Xe) of helium and xenon.

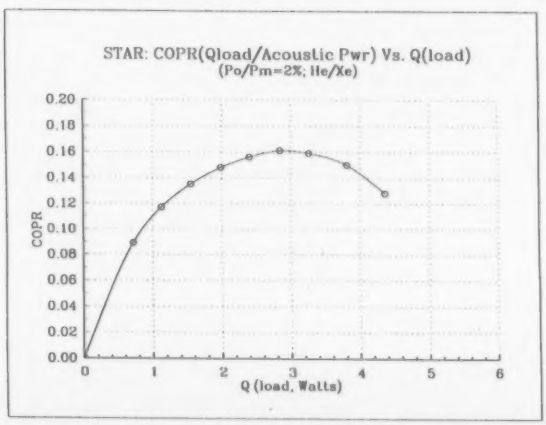

output voltage to a set-point voltage determined by the Controller Board. The difference in the measured and set-point levels produces an error voltage which is electronically integrated and fed back to the automatic gain control input of the voltage controlled oscillator. Both of these control operations are accomplished using analog electronics.

Refrigerator Performance.

The performance of STAR can be summarized by the two graphs which are presented here as Figures 5 and 6. Other measurements of the performance of the entire system, including the electrodynamic driver are included in Reference 16. The performance shown in Figures 5 and 6 is by no means the best which has been achieved in a thermoacoustic refrigerator of this style. Other improvements to the design, such as the use of a stack which has non-uniform spacing, have produced a single-stage, no-load temperature span of 118° K even without the use of gas mixtures to reduce viscous losses or improve the coefficient-of-performance. Coefficients-of-performance relative to Carnot as large as 20% have also been measured.[15]

Further Thermoacoustic Refrigeration Research at NPS

STAR is the first in a series of space-based cryocoolers now under development at the Naval Postgraduate School. Its performance places it between two useful limits. Cryocooler applications generally require relatively little heat pumping power (a watt or less) but a very large temperature span (ΔT = 100 to 200° K). The requirements of residential refrigerator/freezers and air conditioners are opposite of those for spacecraft cryocoolers. Those application require modest temperature spans (ΔT 25 - 45° K), but much higher heat pumping powers, on the order of hundreds of watts for refrigerators and thousands of watts for air conditioners. They also are typically powered by 110 volt alternating current rather than 28 volt direct current. There are several design modifications which are therefore required to adapt this proven thermoacoustic technology to those commercial applications, but these modifications do not present any substantial technological barriers.

At the high temperature span end of the spectrum, a follow-on thermoacoustic space-based cryocooler, TAR-3, is currently under development at NPS with the goal of providing cooling for Hi-T_c superconductors on the HTSSE 2 experiment for the Naval Research Laboratory's Naval Center for Space Technology. For higher heat loads, a thermoacoustic refrigerator/freezer[18] which has heat pumping capabilities similar to a small home refrigerator (200 Watts at 4° C, 120 W at -22° C)[19] is also under development at NPS for the Life Sciences Division of the National Aeronautics and Space Administration.

Acknowledgements

The authors are indebted to Dr. Greg W. Swift, Los Alamos National Labs, for several conversations regarding this new technology and for his excellent review article on thermoacoustic engines[9]. The contents of that review was exploited extensively in the first part of this paper. The development of the Space Thermoacoustic Refrigerator was the work of several staff and students at the Naval Postgraduate School. Staff members include David Rigmaiden (Payload Manager), Glenn Harrell (Machinist), Jim Horning and Ron Phelps (Programmers). The students who worked on the project in partial fulfillment of their Master's degrees were LT Michelle Fitzpatrick, USCG (Driver), LT. Michael Susalla, USN (Thermodynamics and Gas Mixtures), CAPT David Harris, Canadian Forces (Driver), LT Richard Volkert, USN (Driver), and MAJ Ronald Byrnes, USA (Electronics). Additional electronics support was provided by LCDR Charles Cameron, USN.

The loudspeakers used as the drivers were donated by Harmon-JBL and modified by their engineer, Fancher Murray. This work has been supported by the the Office of Naval Research (Physics Division), the Office of Naval Technology, and the Naval Postgraduate School Direct Funded Research Program. Substantial funding and technical support for STAR was provided by the Naval Research Laboratory's Naval Center for Space Technology. We are particularly grateful to Mike Melich for arranging the NPS/NRL collaboration, to Tom Kawecki for providing special services and to Charlie Merk for the design and fabrication of the battery boxes. The payload launch services were provided by the Air Force Space Test Program.

Biographies

Steven L. Garrett received his Ph.D. degree in physics from the University of California at Los Angeles in 1977. Since 1982 he has been at the Naval Postgraduate School where he is now a Professor of Physics. He is currently Principal Investigator on a NAVSEA fiber optic hydrophone project and the ThermoAcoustics Life Sciences Refrigerator which is being developed for NASA under a CRDA with General Electric. Prof. Garrett is a member of the American Physical Society and a fellow of the Acoustical Society of America.

Thomas J. Hofler received his Ph.D. in Physics from the University of California, San Diego, in 1986. Since receiving his degree he has been at the Naval Postgraduate School where he has lead the research effort on thermoacoustic refrigeration. He is the Principal Investigator on the TAR-3 thermoacoustic cryocooler experiment for the Naval Research Laboratory – Center for Space Technology. TAR-3 is designed to reach temperatures below 100 K. Prof. Hofler was the 1990 recipient

of the R.B. Lindsey Award of the Acoustical Society of America for the best acoustician in North America under age thirty-five.

Jay A. Adeff received his B.S. in physics from the University of California at Los Angeles in 1987, and his M.S. in physics from the Naval Postgraduate School in 1990. He has been working at the Naval Postgraduate School with Professors Garrett and Hofler since 1988. He served as engineer and technician on the Space Thermoacoustic Refrigerator (STAR) project, and is not the Principal Engineer on the TAR-3 thermoacoustic cryocooler experiment.

References

1. R. E. Benedick, *Ozone Diplomacy: New Directions in Safeguarding the Planet*, (Harvard University Press, Cambridge, MA, 1991).
2. M. W. Browne, "Cooling with Sound: An Effort to Save Ozone Shield", *The New York Times* (25 Feb 1992), pp. B5 and B9.
3. J. C. Wheatley, T. Hofler, G. W. Swift, and A. Migliori, "Experiments with an Intrinsically Irreversible Acoustic Heat Engine," Phys. Rev. Lett. **50**, 499 (1983); "An Intrinsically Irreversible Thermoacoustic Heat Engine," J. Acoust. Soc. Am. **74**, 153 (1983); "Acoustical heat pumping engine," U. S. Patent No. 4,398,398 (Aug. 16, 1983); "Intrinsically irreversible heat engine," U. S. Patent No. 4,489,553 (Dec. 25, 1984).
4. A. A. Atchley, T. J. Hofler, M. J. Muzzerall, M. D. Kite, C. Ao, "Acoustically generated temperature gradients in short plates", J. Acoust. Soc. Am. **88**(1), 251-263 (1990).
5. A. A. Atchley, H. E. Bass, T. J. Hofler, H-T Lin, "Study of a thermoacoustic prime mover below onset of self-oscillation" J. Acoust. Soc. Am. **91**(2), 734-743 (1992).
6. S. L. Garrett and T. B. Gabrielson, "Magnetohydrodynamic and thermoacoustic mechanisms for generation of sound in seawater", in *Power Transducers for Sonics and Ultrasonics* (Springer-Verlag, 1991), pp. 162-177.
7. J. W. Strutt (Lord Rayleigh), *The Theory of Sound*, 2nd ed., Vol. II (Dover, 1945), §322j.
8. T. Yazaki, A. Tominaga, and Y. Narahara, "Experiments on thermally driven acoustic oscillations of gaseous helium," J. Low Temp. Phys, **41**, 45 (1980).
9. G. W. Swift, "Thermoacoustic engines," J. Acoust. Soc. Am. **84**(4), 1145-1180 (1988).
10. G. W. Swift and S. L. Garrett, "Resonance reciprocity calibration of an ultracompliant transducer", J. Acoust. Soc. Am. **81**(5), 1619-1623 (1987).
11. L. D. Landau and E. M. Lifshitz, *Fluid Mechanics* (Pergamon Press, 1959), §52.
12. In a more complete analysis, there is some mass flux normal to the plate due to the coefficient of thermal expansion of the gas. For a more detailed discussion see N. Rott, "Thermoacoustics", Adv. Appl. Mech. **20**, 135-175 (1980), and references therein.
13. D. A. Harris and R. E. Volkert, "Design and Calibration of an Electrodynamic Driver for the Space Thermoacoustic Refrigerator", Master's Thesis, Naval Postgraduate School, Monterey, CA (Dec. 1989); DTIC Report No. AD A212 022.
14. R. B. Byrnes, Jr., "Electronics for Autonomous Measurement and Control of a Thermoacoustic Refrigerator in a Space Environment", Master's Thesis, Naval Postgraduate School, Monterey, CA (Dec. 1989); DTIC Report No. AD B141 388.
15. M. P. Susalla, "Thermodynamic Improvements for the Space Thermoacoustic Refrigerator", Master's Thesis, Naval Postgraduate School, Monterey, CA (June, 1988); DTIC Report No. AD A196 958.
16. J. A. Adeff, "Measurement of the Space Thermoacoustic Refrigerator Performance", Master's Thesis, Naval Postgraduate School, Monterey, CA (Sept. 1990); DTIC Report No. AD A241 320.
17. T. Hofler, "Accurate acoustic power measurements with a high-intensity driver," J. Acoust. Soc. Am. **83**(2), 777-786 (1988).
18. S. Garrett, "ThermoAcoustic Life Sciences Refrigerator", NASA Tech. Report No. LS-10114, L. B. Johnson Space Center, Space and Life Sciences Directorate, Houston, TX (October 30, 1991).
19. LSLE Refrigerator/Freezer: Specifications and Assembly Drawing (S/AD), NASA Tech. Report No. LS-30063, L. B. Johnson Space Center, Space and Life Sciences Directorate, Houston, TX (September 8, 1982).

Research Notes

Navy Honors Dr. Robert Ballard for Scientific Achievement

Dr. Robert D. Ballard is this year's recipient of the Robert Dexter Conrad Award, the Navy's highest honor for scientific achievement. The Honorable Gerald A. Cann, Assistant Secretary of the Navy for Research, Development and Acquisition, presented the award, in the form of a gold medal and certificate, at a ceremony in his office on June 15.

Dr. Ballard is Director of the Center for Marine Exploration and Senior Scientist of the Deep Submergence Laboratory, Woods Hold Oceanographic Institution, Woods Hole, Massachusetts. In these capacities, he directs advanced, deep-water exploration technology aimed at better understanding the ocean floor with special emphasis on the Mid-Ocean Ridge.

The Conrad Award is presented annually to an individual who has made outstanding contributions in scientific research and development for the Department of the Navy. It commemorates Captain Robert Dexter Conrad, who was one of the primary architects of the Office of Naval Research (ONR), the R&D organization responsible for the basic research programs of the Navy.

Since 1967, Dr. Ballard has been an ONR contractor primarily in the fields of deep ocean engineering and marine geology. He is also founder and director of the JASON-Foundation for Education, Waltham, Massachusetts, which focusses on stimulating high school students to participate in and follow careers in science.

Under a series of ONR and Office of Naval Technology grants, Dr. Ballard pioneered the development of remote, unmanned, intelligent underwater vehicles, such as the famous robot Jason, with its high-quality cameras and advanced manipulators. The Testing expedition of Jason and Argo, it's camera platform, began in 1985 with the discovery of the wreck RMS Titanic at a depth of 3,795 meters in the North Atlantic; later, complicated testing maneuvers were done successfully within the wreck. As the acknowledged leader in this field, the Navy granted Dr. Ballard the title of Secretary of the Navy Chair in Oceanography (1985-1989) with it's accompanying stipend to continue and expand his research program.

Dr. Ballard is the 36th Conrad Award winner. His other awards and honors include: Underwater Society of America Science Award, Marine Technology Society Distinguished Achievement Award, the Sigma Xi William Proctor Award, the Newcomb-Cleveland Award from AAAS, and nine honorary doctorate degrees. He has authored over 50 articles and scientific papers as well as eight books.

In 1965, Dr. Ballard graduated from the University of California. Later, he did graduate work at the Universities of Hawaii and Southern California, and received his Ph.D. from the University of Rhode Island.

New and Powerful Laser

Vanderbilt University recently dedicated a new free-electron laser (FEL), the most powerful laser of its type in the world. This laser was made possible through funding by the Office of Naval Research. The free-electron laser was purchased through a $9 million ONR contract, which was followed by a $5.7 million ONR contract to support research projects using the laser.

Unlike conventional lasers, a FEL can be tuned to a variety of wavelengths and can produce particularly high-intensity light beams. The FEL promises benefits in such applications as microelectronics; production of materials not found in nature; fundamental studies in physics, chemistry, biology and electrical engineering; and clinical applications throughout medicine.

To produce the energy from a FEL, accelerators project electrons at 45 million volts into a magnetic field designed to make the electrons "wiggle." For comparison, a television set uses 15,000 volts. When the electrons wiggle, they give off radiation. Because they are moving close to the speed of light, the radiation shows up in the infrared part of the spectrum.

Conventional lasers produce light by exciting electrons in a solid, liquid or gas.

The FEL is housed in a vault in a two story facility containing 13,000 square feet, all of which is underground. A series of pipes and mirrors guides the beam from the laser to the laboratories located on the top floor of the facility. The wavelength of the FEL is controlled by a computer, and researchers can manipulate the laser at a computer in their laboratory.

Researchers at the FEL site are now at work. One team is studying how computer imaging can be used to guide the laser for the precision needed to treat a malignant brain cancer. Another research group is moving toward a new form of X-rays that requires only 1/50th of the current dose of radiation needed to provide a high-quality image. A physicist is exploring the interactions of intense laser light with different types of matter to better understand lightwave technology.

In the future, the FEL center will have available monochromatic X-rays with energy tunable over the range from 1 to 20 kilovolts, and a far-infrared laser tunable to wavelengths in the range from 50 to 200 micrometers. This will give the Vanderbilt center the broadest range of tunable radiation of any facility in the world.

Bubbles May Help Us See Underwater

Bubbles produced by waves can be harnessed by a revolutionary new sonar that could be used to reveal ocean objects such as the nets of trawlers, Arctic ice hazards, and other threats to submarines. This concept named "acoustic daylight" is based on sounds created by churning waves. Michael J. Buckingham of Scripps Institution of Oceanography and Stewart Glegg of Florida Atlantic University developed this new technology through Office of Naval Research funding. The idea itself is not new, but it is the first time the principle has been demonstrated by practical experiment.

The sounds produced by the air bubbles spread throughout the ocean's depths producing a natural, ambient field of noise. Like daylight, the noise is uniform until it hits an object. By using computer imaging to sketch an object such as a fish, reef, or sunken ship, that disturbs the ambient noise, the image appears on a video screen a few moments later. If fully developed, this video technology could aid underwater construction and repair; be used as a surveillance camera or security device; and might protect harbor entrances from quiet submarines.

"It's actually the bubbles that create the noise, a sort of ringing at the point of closure when a bubble becomes a globule of air surrounded by water. At that point, it begins to oscillate in and out," Buckingham said. The moment, which some scientists have described as the bubble's "birth yell," lasts only a few milliseconds. Then the bubble is silent forever. The sound of that momentary oscillation lingers; however, it is multiplied and magnified by uncountable bubbles created continuously by the ocean's movement against the object. Once created, the sound is dispersed into the ocean's depths, and there is little deterioration of the sound in deep water because the sound has nowhere to go. The result is comparable to sunlight, which spreads out to fill all of the space available equally.

The tool used in these experiments is a concave acoustic mirror similar to the light-gathering mirrors used in astronomical telescopes. Four feet in diameter, it is parabolically shaped and coated with thick neoprene. A microphone, shielded against sound coming from directions other than the reflector, is mounted at the focus of the parabolic dish to measure the intensity of sound concentrated at the spot. Without generating any noise of its own, the device easily detected the presence of test objects within its field of view.

"The acoustic daylight system is still in the very early stages of research," said Marshall Orr, program manager of ONR's Ocean Acoustic Program. "But the results are quite good for the investment."

DEPARTMENT OF THE NAVY
OFFICE OF NAVAL RESEARCH
ARLINGTON, VA 22217

OFFICIAL BUSINESS
PENALTY FOR PRIVATE USE, $300